Supporting Information

Boosting Electrocatalytic CO_2 Reduction Reaction over Viologen Functionalized Metal-Organic Frameworks by Enhancement of Electro Transfer Capacity

Yu-Liang Dong[1,2], Zi-Yan Jing[1,2], Qiu-Jin Wu[2], Zi-Ao Chen[2], Yuan-Biao Huang[1,2,3,4]* and Rong Cao[1,2,3,4]*

[1] College of Chemistry, Fuzhou University, Fujian, 350108, P. R. China

[2] State Key Laboratory of Structural Chemistry, Fujian Institute of Research on the Structure of Matter, Chinese Academy of Sciences, Fuzhou, 350002, Fujian

[3] University of Chinese Academy of Science, Beijing 100049

[4] Fujian Science & Technology Innovation Laboratory for Optoelectronic Information of China, Fuzhou, 350108, Fujian

*Corresponding Author(s): ybhuang@fjirsm.ac.cn; rcao@fjirsm.ac.cn

Section 1. Material and Methods

All regents and chemicals were purchased without further purification.

Powder X-ray diffraction (PXRD) patterns were recorded on a Miniflex 600 diffractometer using Cu Kα radiation (λ = 0.154 nm). N_2 adsorption-desorption isotherm and the Brunauer-Emmett-Teller (BET) surface area measurements were measured by using Micromeritics ASAP 2460 instrument at 77 K. CO_2 adsorption-desorption isotherms were measured by using Micrometrics ASAP 2020 instrument at 298 K. Infrared (IR) spectra were recorded using KBr pellets on a PerkinElmer Spectrum One in the range of 400-4000 cm^{-1}. 1H NMR and Solid-state ^{13}C NMR spectras was performed at AVANCE III BrukerBiospin spectrometer, operating at 400 MHz. X-ray photoelectron spectroscopy (XPS) measurements were performed on an ESCALAB 250Xi X-ray photoelectron spectrometer (Thermo Fisher) using an Al Ka

source (15 kV, 10 mA). Elemental analyses of C, H, N and were carried out on an Elementar Vario EL III analyzer. Thermogravimetric analyses (TGA) were performed under nitrogen atmosphere with heating rate of 10 °C min^{-1} to 800 °C by using an SDT Q600 thermogravimetric analyser. Analysis of Co content in Por(Co)-MOF and Vg-Por(Co)-MOF(n : 1) (n=1, 2, 5, 9) were measured by inductively coupled plasma atomic emission spectroscopy (ICP-AES) on an Ultima 2 analyzer (Jobin Yvon). Scanning electron microscope (SEM) was recorded by a FEIT 20 working at 10 kV. Transmission electron microscope (TEM) images were taken on a FEI TECNAI G2 F20 microscope equipped EDS detector at an accelerating voltage of 200 kV. Atomic Force Microscope (AFM) images were recorded on Bruker Dimension Icon. XAFS measurement and data analysis: XAFS spectra of the Co K-edge were collected at BL14W1 station in Shanghai Synchrotron Radiation Facility (SSRF). The Co K-edge XANES data were recorded in a transmission mode. The gas chromatography measurements were performed on the Agilent 7820A gas chromatograph (GC) equipped with FID and TCD. ATR-FTIR experiments were performed on a Nicolet6700 (Thermo Fisher) equipped a liquid nitrogen cooled MCT detector. $^{13}CO_2$ isotope trace analysis was conducted on Shimadzu GCMS-QP2020 Gas Chromatograph Mass Spectrometer. To estimate the ECSA, CV were tested by measuring Cdl under the potential window range from -0.15 V to −0.25 V (vs. RHE) with various scan rates from 10 to 100 mV s^{-1}. All the LSV curves were presented without iR compensation. Tafel plots for the CO production over Por(Co)-MOF, Vg-MOF and Vg-Por(Co)-Vg-MOF(n : 1) (n = 1, 2, 5, 9) were performed in the 0.5 M $KHCO_3$ electrolyte solution, which were calculated from the corresponding overpotentials versus $\log|j_{CO}|$.

H-type cell:

The electrochemical measurements were performed in a H-type cell with two compartments separated by a anion exchange membrance (Nafion-117) by chi700e at room temperature One compartment contained 70 mL electrolyte (0.5 M $KHCO_3$ aqueous solution made from DI water) and Pt foil as counter electrodes, another with the same electrolyte, Ag/AgCl electrode in saturated KCl solution as reference

electrodes and working electrode. Typically, 5 mg of the catalyst and 3 mg ketjenblack were dispersed in 480 μL of isopropanol and 20 μL of Nafion binder solution (5 wt%) under sonication for 1 h to form a homogeneous ink. Then 100 μL of the catalyst ink was loaded onto the carbon fiber paper electrode with 1×1 cm^2. During the electrochemical measurements, the electrolyte solution was purged with CO_2 for 30 min to achieve the CO_2-saturated solution (pH = 7.6). Linear sweep voltammetry (LSV) was performed with a scan rate of 10 mV s-1 from 0 V to -1.2 V vs. RHE in CO_2-saturated 0.5 M $KHCO_3$ electrolyte. All measured potentials were converted to reversible hydrogen electrode (RHE) scale using the following equation: E(vs. RHE)= E(vs. Ag/AgCl) + 0.059 pH + 0.197 V. CO_2 gas was delivered at an average rate of 30 ml/min (at room temperature and ambient pressure) and routed into the gas sampling loop (0.8 mL) of a gas chromatograph. The gas phase composition was analyzed by GC every 15 min. The separated gas products were analyzed by a thermal conductivity detector (for H_2) and a flame ionization detector (for CO, CH_4). The liquid products were analyzed afterwards by quantitative NMR (Bruker AVANCE AV III 400). Solvent presaturation technique was implemented to suppress the water peak.

MEA cell:

Electrochemical measurements with high current densities were performed in a MEA cell. An as-prepared gas-diffusion electrode (1 cm * 1 cm) was employed as the cathode, and a polytetrafluoroethylene (PTFE) insulator sheet with a 1 cm^2 window was attached to the cathode to avoid short circuit. A pre-treated Versogen membrane (A20-HCO_3, 1.5 cm * 1.5 cm) and Ni foam (1 cm * 1 cm) were put on the top of the membrane. Then, 1 M KOH aqueous solution was used as the anolyte and circulated using a pump at a rate of 10 mL/min. On the cathode side, CO_2 gas (30 sccm) was continuously humidified with DI water and fed into the cathode chamber. The performance of the catalysts in an MEA system was evaluated by applying different cell voltages using an chi760e electrochemical workstation. Linear sweep voltammetry (LSV) was performed with a scan rate of 10 mV s^{-1} from the cell voltage1 to 3 V. During electrolysis procedure, the effluent gas from the cathode compartment went through the sampling

loop (1 mL) of a gas chromatograph. The gas phase composition was analyzed by GC every 15 min. The separated gas products were analyzed by a thermal conductivity detector (for H_2) and a flame ionization detector (for CO).

Faradic efficiency:

The Faradaic efficiency (FE) for CO production at each applied potential was calculated based on the following equations:

$$FE = \frac{j_{CO}}{j_{total}} = \frac{v_{CO} \times N \times F}{j_{total}}$$

FE: Faradaic efficiency for CO production (%);

j_{CO}: partial current density for CO production;

j_{total}: total current density;

v_{CO}: the production rate of CO;

N: the number of electron transferred for product formation. Here, it is 2 for CO;

F: Faradaic constant number: 96485 C mol^{-1}.

Turnover frequency (h^{-1}):

The turnover frequency (TOF, h^{-1}) for CO was calculated based on the following equations:

$$TOF = \frac{I_{total} \times FE_{CO}}{N \times F \times n_{total}} \times 3600$$

I_{total}: total current;

FE: Faradaic efficiency for CO production (%);

N: the number of electron transferred for product formation (here, it is 2 for CO);

F: Faradaic constant, 96485 C mol^{-1};

n_{total}: the total moles of metal employed in the electrolysis.

Measurement of conductivity:

To make a pressed pellet, the MOF sample was put into a 6 mm inner-diameter split sleeve pressing die and pressed for 5 min under a pressure of approximately 1000 psi. A two-contact probe method was employed to collect bulk conductivity measurements of the MOFs pellet. The two-contact probe method is easy to configure and is suitable for the conductivity measurement of resistive samples. We calculated the bulk conductivity measurements (S/cm) using the following equations. Herein, L is the distance of between the probes, which equals the thickness of the pellet, A is the basal area of the pellet, V (volts) is the voltage of cross the probes, I (A) is current, which is measured by a potentiostat.

$$\sigma = \frac{IL}{VA}$$

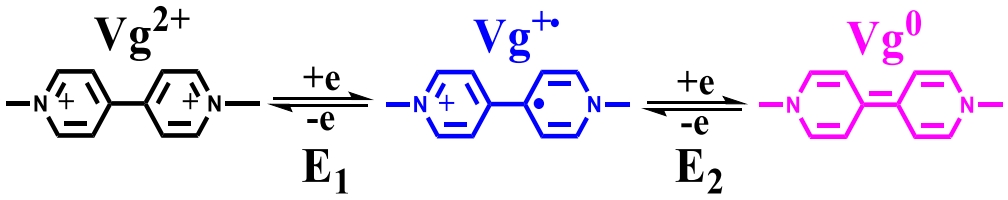

Figure S1. Electrochemical reversible redox activity of Viologen groups.

Section S2. Ligand Synthesis

Synthesis of 5, 15-di(p-benzoato)porphyrin (MePor):

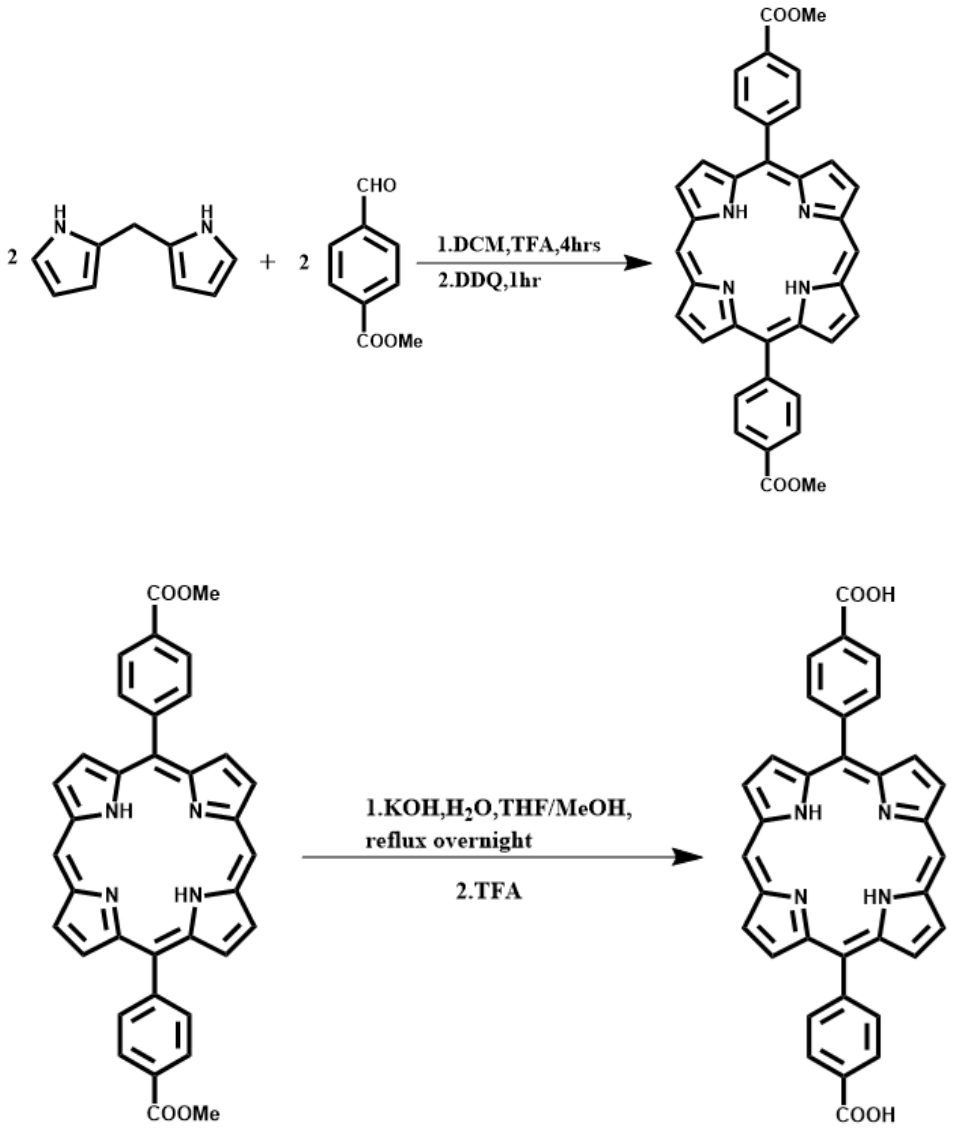

Scheme S1. Synthesis of the 5, 15-di(p-benzoato)porphyrin ligand.

4-(Methoxycarbonyl)benzaldehyde (1.20 g, 7.3 mmol) and dipyrrylmethane (1.07 g, 7.3 mmol) were added to a round bottom flask. To the flask 1 L of anhydrous dichloromethane (DCM) was added. Trifluoroacetic acid (0.34 mL, 4.4 mmol) was added dropwise via a syringe. The mixture was stirred at room temperature for 4 hours. To the reaction mixture, 2.49 g 2,3-dichloro-5,6-dicyano-1,4-benzoquinone (DDQ, 11.0 mmol) was then added and the mixture was stirred for another hour. Triethylamine was added to neutralize the reaction mixture. The solvent was removed with a rotary evaporator, and the 5, 15-di(p-methyl-benzoato)porphyrin (MePor) product was

purified by column chromatography with chloroform as the eluent. Yield: 810 mg, 1.40 mmol (38%). 1H-NMR (500 MHz, chloroform-D, ppm): δ=10.38 (s, 2H), 9.45 (d, 4H), 9.06 (d, 4H), 8.52 (d, 4H), 8.39 (d, 4H), 4.16 (s, 6H), -3.12 (s, 2H).

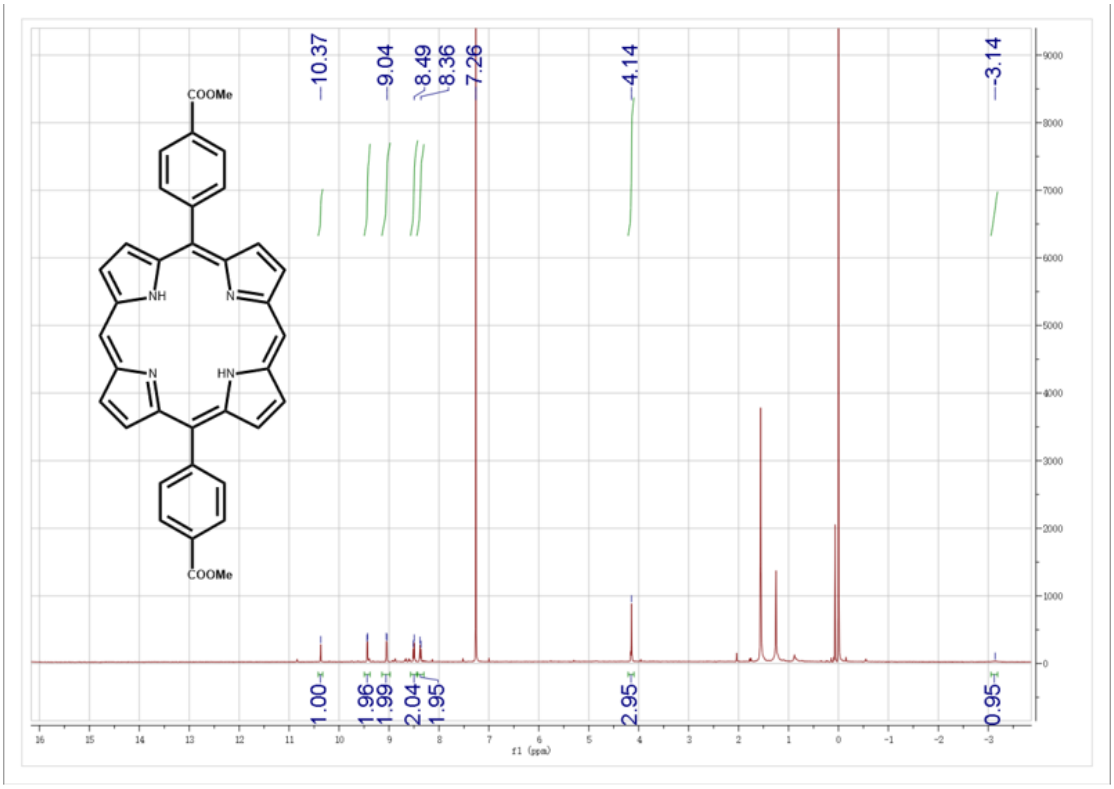

Figure S2. Top, ^{1}H NMR spectrum of 5, 15-di(p-methyl-benzoato)porphyrin in chloroform-D.

The aforementioned MePor (399 mg, 0.69 mmol) was dissolved in a mixture of tetrahydrofuran (THF) and methanol (90 mL, 1:1 vol/vol). A potassium hydroxide aqueous solution (14 mL, 2 M) was then added. The solution was heated to reflux under nitrogen protection overnight. Half of the solvent was removed with a rotary evaporator before the solution was neutralized to pH=3 with trifluoroacetic acid. The dark purple product was collected by centrifugation and washed with water and ether. The solid residue was dried under vacuum to give the pure Por product in 95% yield (362 mg, 0.66 mmol). 1H-NMR (500 MHz, DMSO-D6, ppm): δ=13.35 (s, 2H), 10.71 (s, 2H), 9.71 (d, 4H), 9.08 (d, 4H), 8.45 (m, 8H), -3.26 (s, 2H).

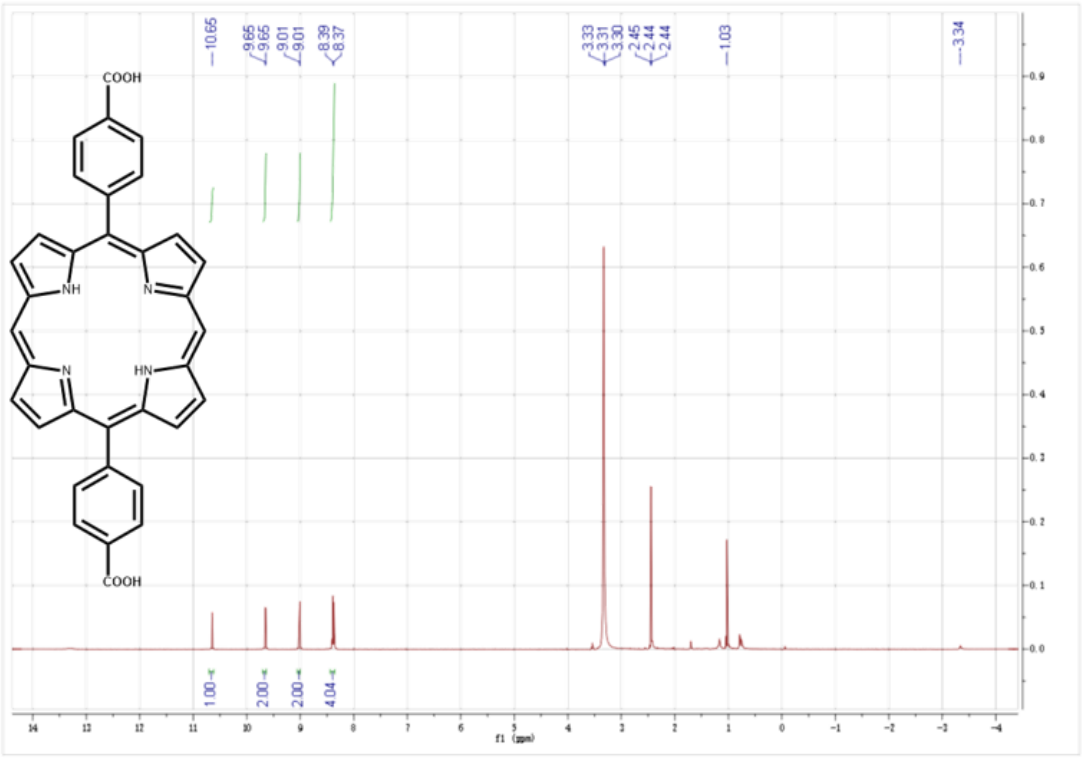

Figure S3. Top, ^{1}H NMR spectrum of 5, 15-di(p-benzoato)porphyrin in DMSO-D6.

Synthesis of 5, 15-di(p-benzoato)porphinato cobalt(II) (Por(Co)):

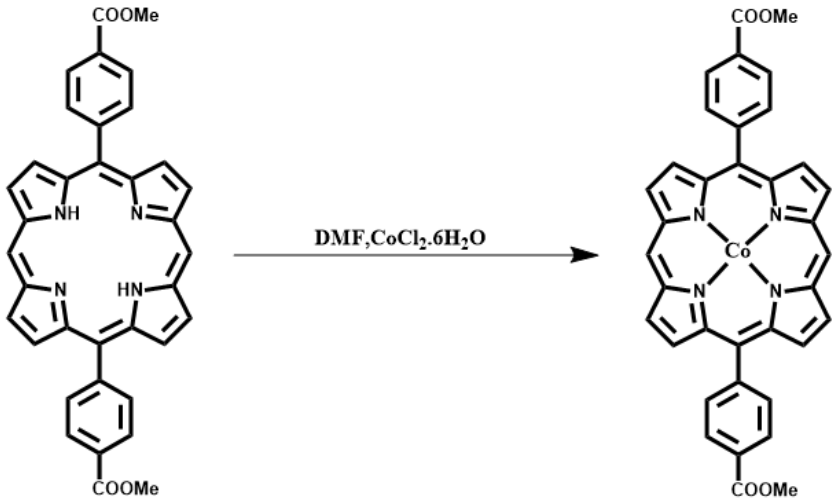

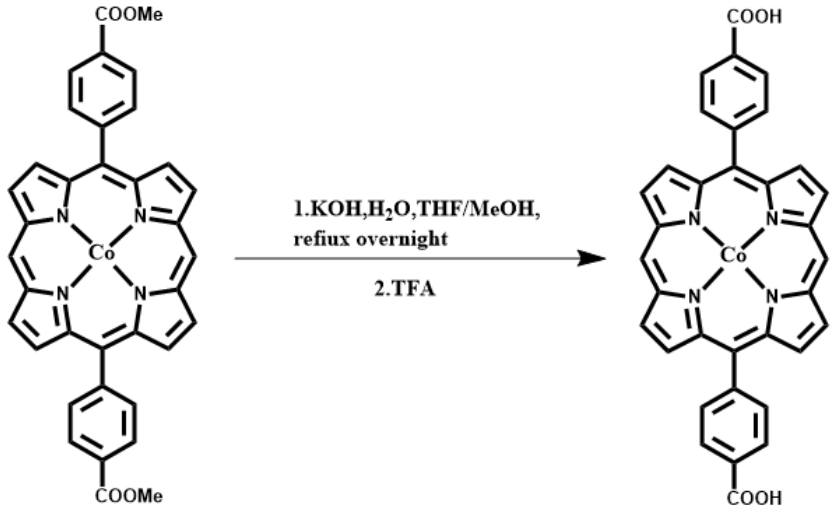

Scheme S2. Synthesis of the 5, 15-di(p-benzoato)porphinato cobalt(II)(Por(Co)) ligand.

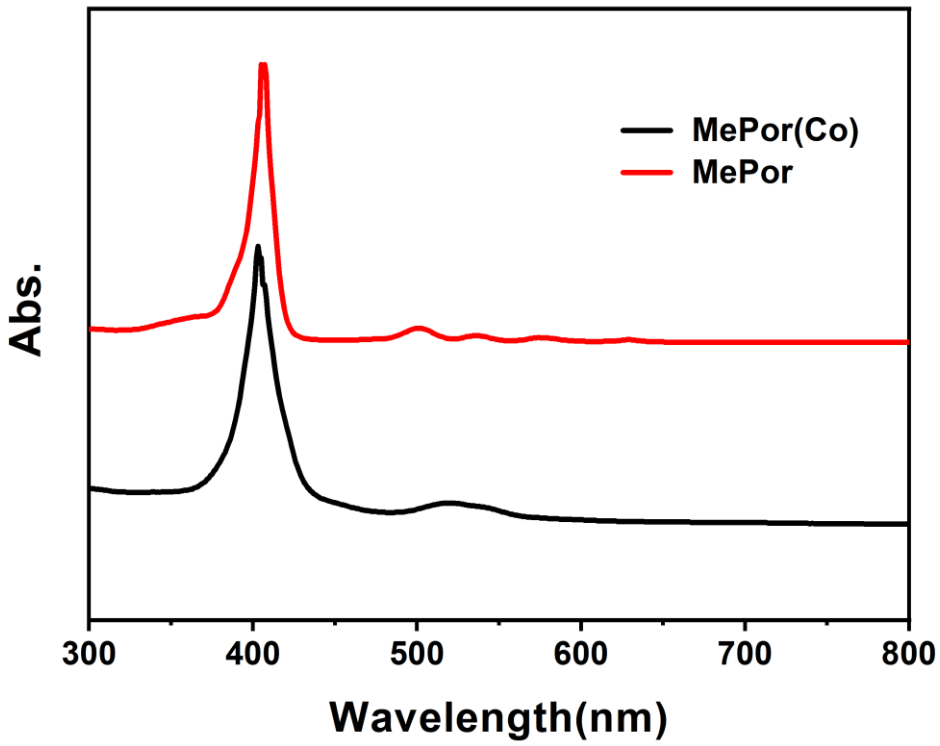

Figure S4. UV-Vis absorption spectra of MePor (red line) and MePor(Co) (black line).

Synthesis of $[H_2bpybdc]Cl_2$ (Vg):

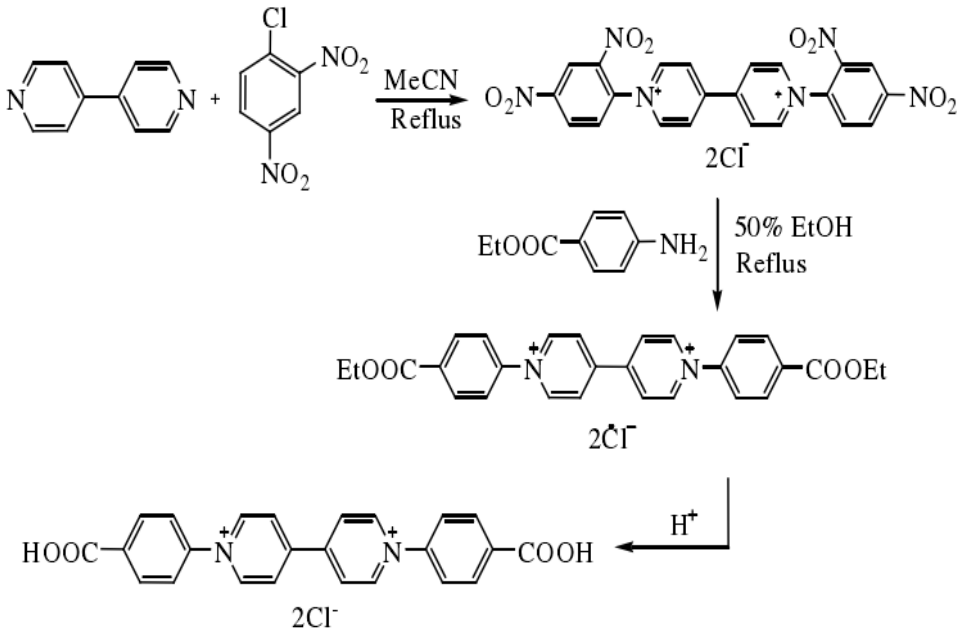

Scheme S3. Synthesis of the $[H_2bpybdc]Cl_2$ (Vg) ligand.

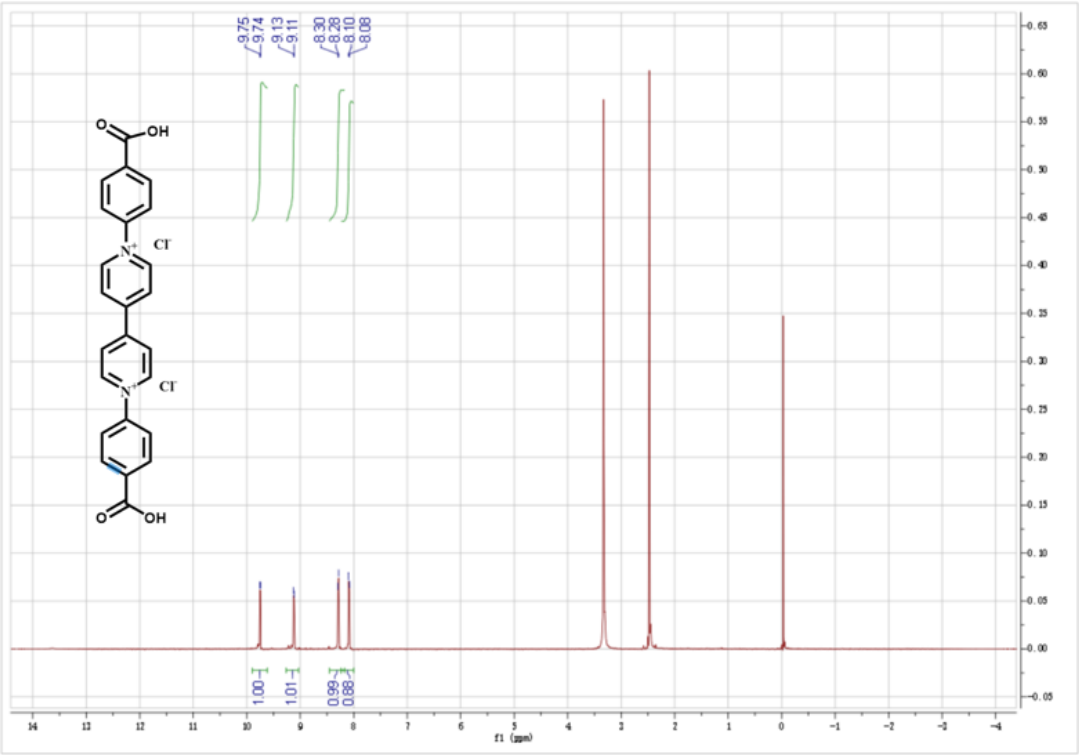

Figure S5. Top, ^1H NMR spectrum of $[H_2bpybdc]Cl_2$ in DMSO-D6.

Synthesis of Paraquatdiiodide:

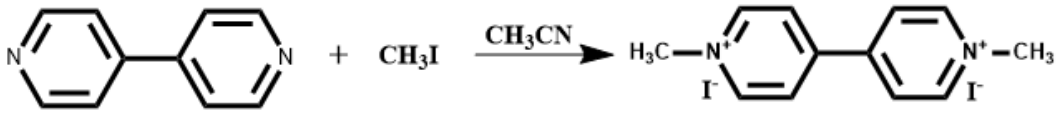

Scheme S4. Synthesis of the Paraquatdiiodide.

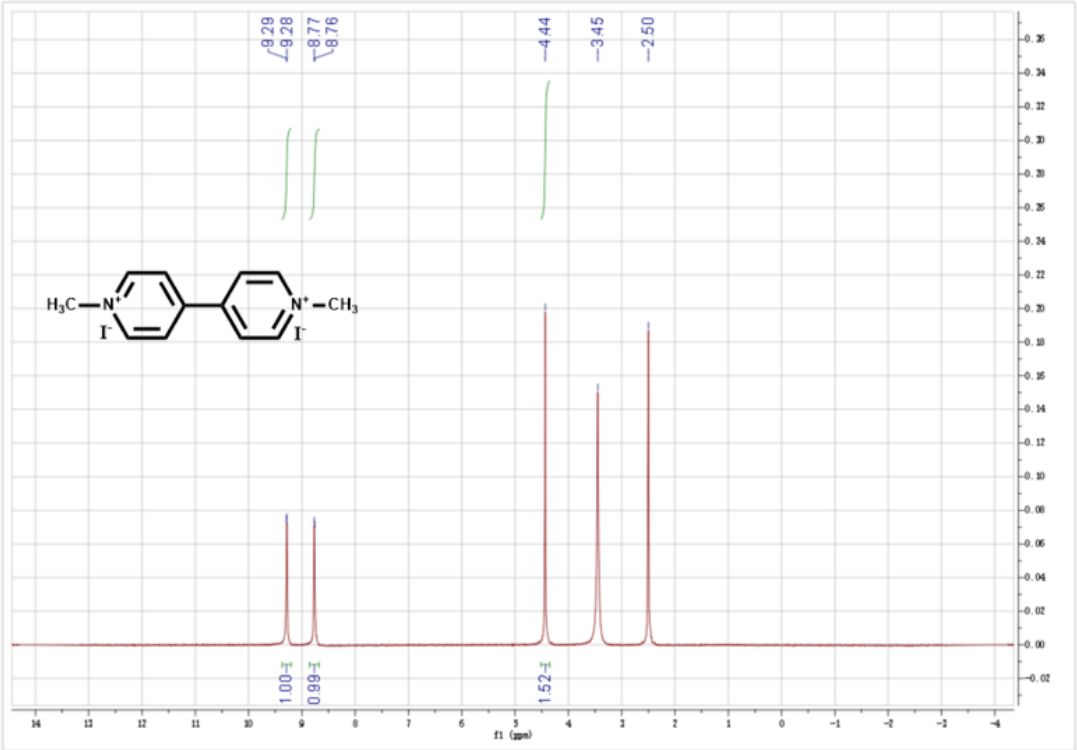

Figure S6. Top, ^{1}H NMR spectrum of Paraquatdiiodide in DMSO-D6.

Section S3. Synthesis of MOFs by mixed ligand strategy:

(1) Synthesis of Vg-MOF:

$ZrOCl_2 \cdot 8H_2O$ (0.024mmol, 8mg), $[H_2bpybdc]Cl_2$ (Vg) (0.034mmol, 16mg) were ultrasonically dissolved in a mixture of 4ml DMF and 2ml H_2O, and TFA (80ul) was then added to the solution in a 20ml glass vial. The vial was then heated at 100 ºC for 72h in an oven. After cooling to room temperature, yellow crystals of Vg-MOF were harvested by filtration. The as-synthesized crystals were washed with fresh DMF (10ml×3) and immersed into another 10ml of DMF at 80 ºC for 48h, when the DMF

was refreshed every 12h. Acetone was finally used to wash the sample before drying.

(2) Synthesis of Por(Co)-MOF:

$HfCl_4$ (0.030mmol, 9.6mg), Por(Co) (0.030mmol, 18.3mg) were ultrasonically dissolved in a mixture of 4ml DMF and 2ml H_2O,and TFA (40ul) was then added to the solution in a 20ml glass vial. The vial was then heated at 100 ºC for 48h in an oven. After cooling to room temperature, dark purple crystals of Por(Co)-MOF were harvested by filtration. The as-synthesized crystals were washed with fresh DMF (10ml×3) and immersed into another 10ml of DMF at 80 ºC for 48h, when the DMF was refreshed every 12h. Acetone was finally used to wash the sample before drying.

(3) Synthesis of Vg-Por(Co)-MOF(9:1):

$HfCl_4$ (0.03mmol, 9.6mg), Por(Co) (0.027mmol, 16.47mg), $[H_2bpybdc]Cl_2$ (Vg) (0.003mmol, 1.41mg) were ultrasonically dissolved in a mixture of 4ml DMF and 2ml H_2O, and TFA (40ul) was then added to the solution in a 20ml glass vial. The vial was then heated at 100 ºC for 48h in an oven. After cooling to room temperature, dark purple crystals of Vg-Por(Co)-MOF(9:1) were harvested by filtration. The as-synthesized crystals were washed with fresh DMF (10ml×3) and immersed into another 10ml of DMF at 80 ºC for 48h, when the DMF was refreshed every 12h. Acetone was finally used to wash the sample before drying.

(4) Synthesis of Vg-Por(Co)-MOF(5:1):

$HfCl_4$ (0.03mmol, 9.6mg), Por(Co) (0.025mmol,15.25mg), $[H_2bpybdc]Cl_2$ (Vg) (0.05mmol, 2.35mg) were ultrasonically dissolved in a mixture of 4ml DMF and 2ml H_2O, and TFA (40ul) was then added to the solution in a 20ml glass vial. The vial was then heated at 100 ºC for 48h in an oven. After cooling to room temperature, dark purple crystals of Vg-Por(Co)-MOF(5:1) were harvested by filtration. The as-synthesized crystals were washed with fresh DMF (10ml×3) and immersed into another 10ml of DMF at 80℃ for 48h, when the DMF was refreshed every 12h. Acetone was finally used to wash the sample before drying.

(5) Synthesis of Vg-Por(Co)-MOF(2:1):

$HfCl_4$ (0.03mmol, 9.6mg), Por(Co) (0.018mmol, 11mg), $[H_2bpybdc]Cl_2$ (Vg) (0.009mmol, 4.7mg) were ultrasonically dissolved in a mixture of 4ml DMF and 2ml H_2O, and TFA (40ul) was then added to the solution in a 20ml glass vial. The vial was then heated at 100℃ for 48h in an oven. After cooling to room temperature, dark purple crystals of Vg-Por(Co)-MOF(2:1) were harvested by filtration. The as-synthesized crystals were washed with fresh DMF (10ml×3) and immersed into another 10ml of DMF at 80℃ for 48h, when the DMF was refreshed every 12h. Acetone was finally used to wash the sample before drying.

(6) Synthesis of Vg-Por(Co)-MOF(1:1):

$HfCl_4$ (0.03mmol, 9.6mg), Por(Co) (0.015mmol, 9.15mg), $[H_2bpybdc]Cl_2$ (Vg) (0.015mmol, 7.05mg) were ultrasonically dissolved in a mixture of 4ml DMF and 2ml H_2O, and TFA (40ul) was then added to the solution in a 20ml glass vial. The vial was then heated at 100℃ for 48h in an oven. After cooling to room temperature, dark purple crystals of Vg-Por(Co)-MOF(1:1) were harvested by filtration. The as-synthesized crystals were washed with fresh DMF (10ml×3) and immersed into another 10ml of DMF at 80℃ for 48h, when the DMF was refreshed every 12h. Acetone was finally used to wash the sample before drying.

(7) Synthesis of MV@Por(Co)-MOF(9:1):

$HfCl_4$ (0.03mmol, 9.6mg), Por(Co) (0.027mmol, 16.47mg), Methyl Viologen (MV) (0.003mmol, 1.32mg) were ultrasonically dissolved in a mixture of 4ml DMF and 2ml H_2O,and TFA (40ul) was then added to the solution in a 20ml glass vial.The vial was then heated at 100 ºC for 48h in an oven.After cooling to room temperature, dark purple crystals of MV@Por(Co)-MOF were harvested by filtration. The as-synthesized crystals were washed with fresh DMF (10ml×3) and immersed into another 10ml of DMF at 80℃ for 48h, when the DMF was refreshed every 12h. Acetone was finally used to wash the sample before drying.

Supporting Figures and Tables:

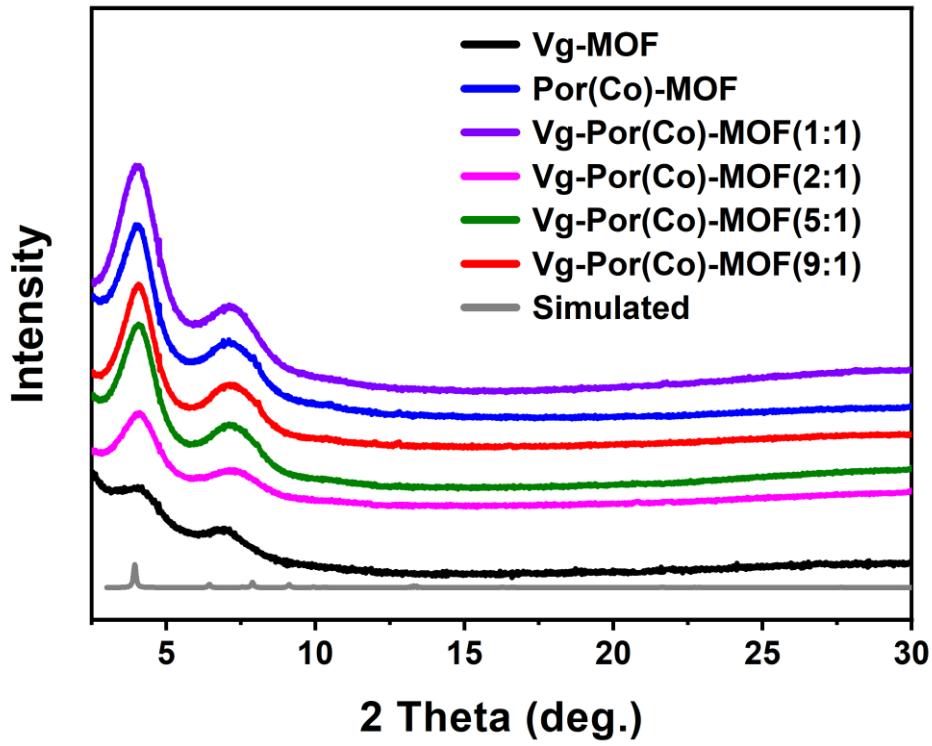

Figure S7. Synchrotron radiation experimental PXRD patterns for Vg-MOF, Por(Co)-MOF, Vg-Por(Co)-MOF(1:1), Vg-Por(Co)-MOF(2:1), Vg-Por(Co)-MOF(5:1), Vg-Por(Co)-MOF(9:1), and simulated patterns for Zn-DPDBP-UiO.

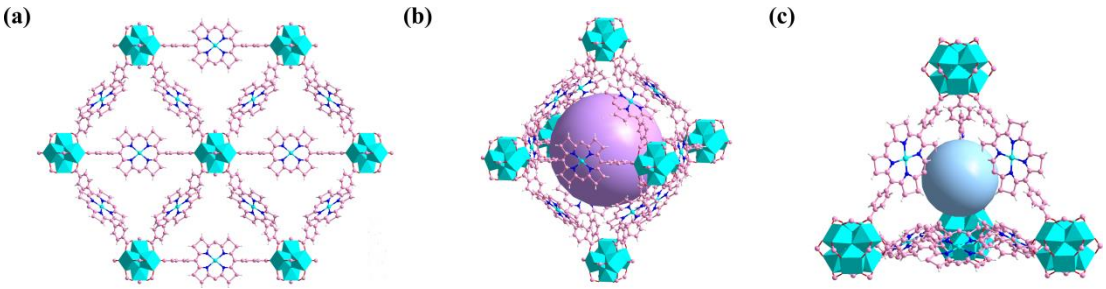

Figure S8. Single-crystal X-ray structure of Por(Co)-MOF. (a) The structure viewed from the [110] direction; (b) the octahedral cavity in the structure; (c) the tetrahedral cavity in the structure.

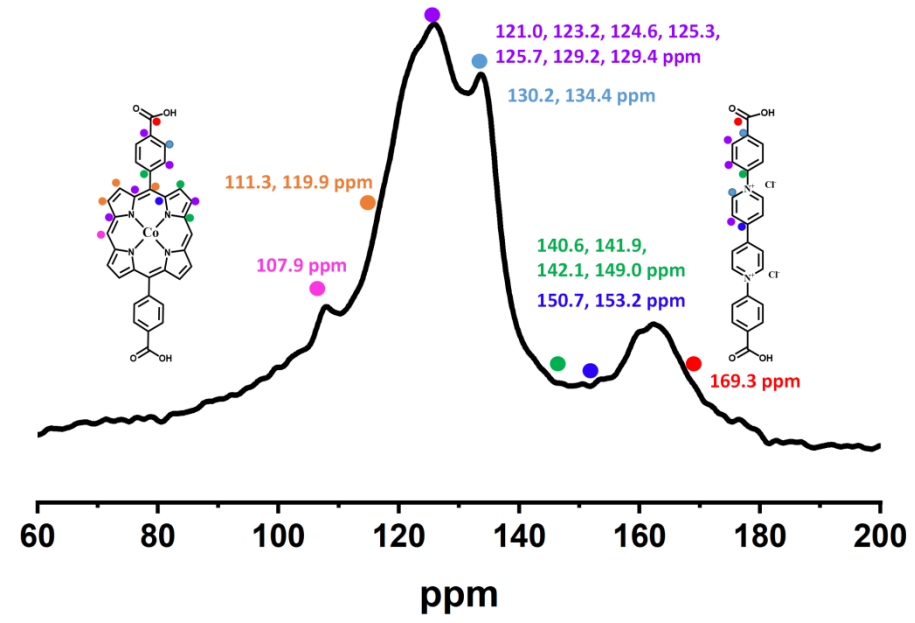

Figure S9. Solid-state ^{13}C NMR spectra of Vg-Por(Co)-MOF(9:1).

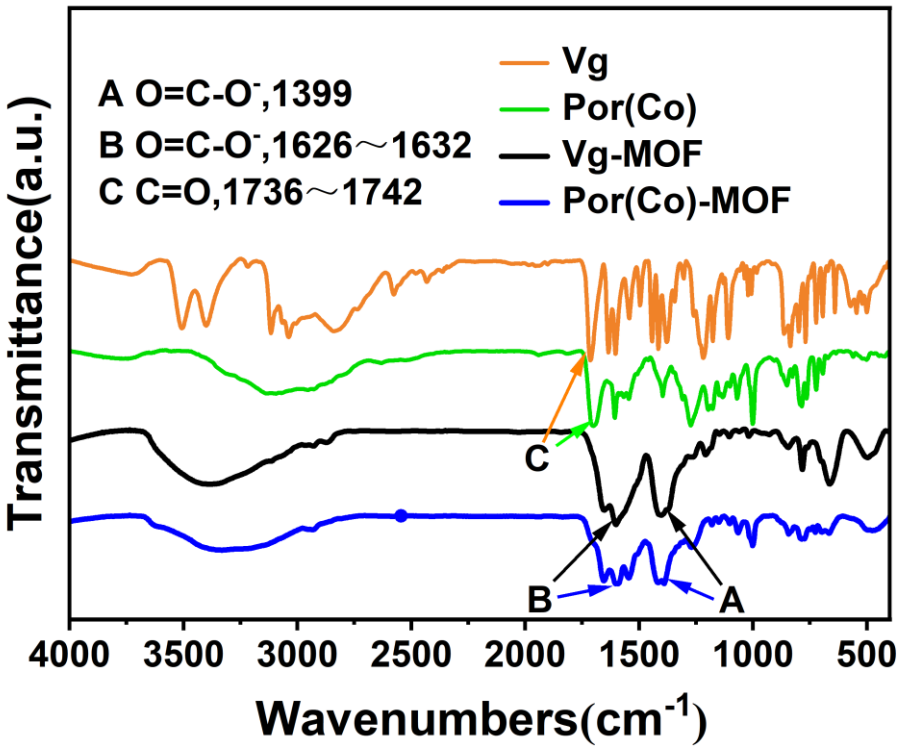

Figure S10. FT-IR spectra of Vg, Por(Co), Vg-MOF and Por(Co)-MOF.

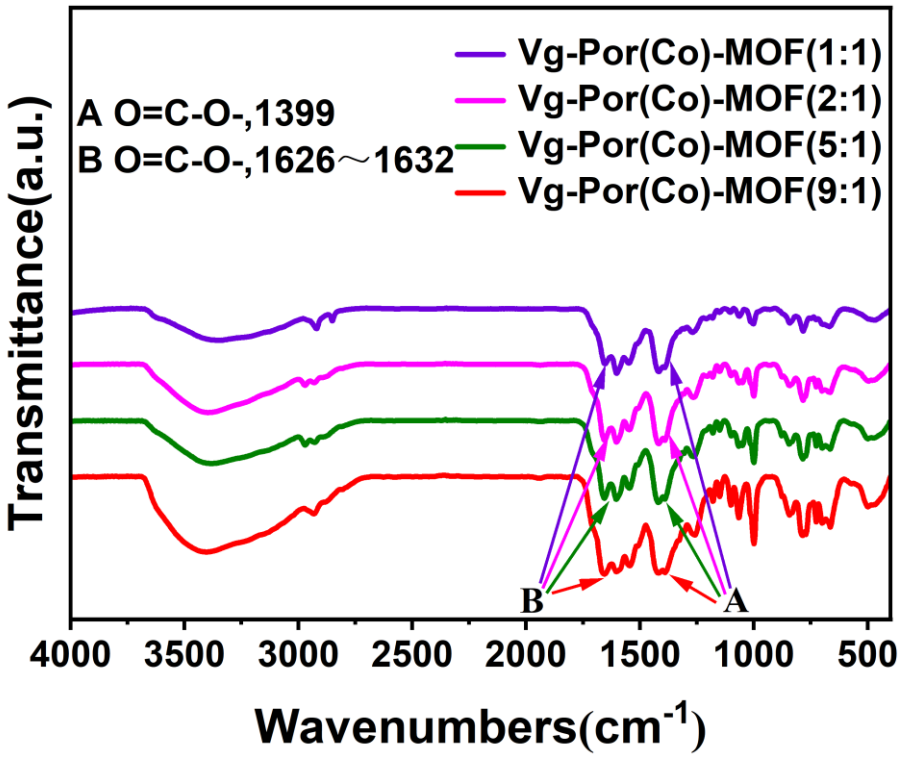

Figure S11. FT-IR spectra of Vg-Por(Co)-MOF(1:1), Vg-Por(Co)-MOF(2:1), Vg-Por(Co)-MOF(5:1) and Vg-Por(Co)-MOF(9:1).

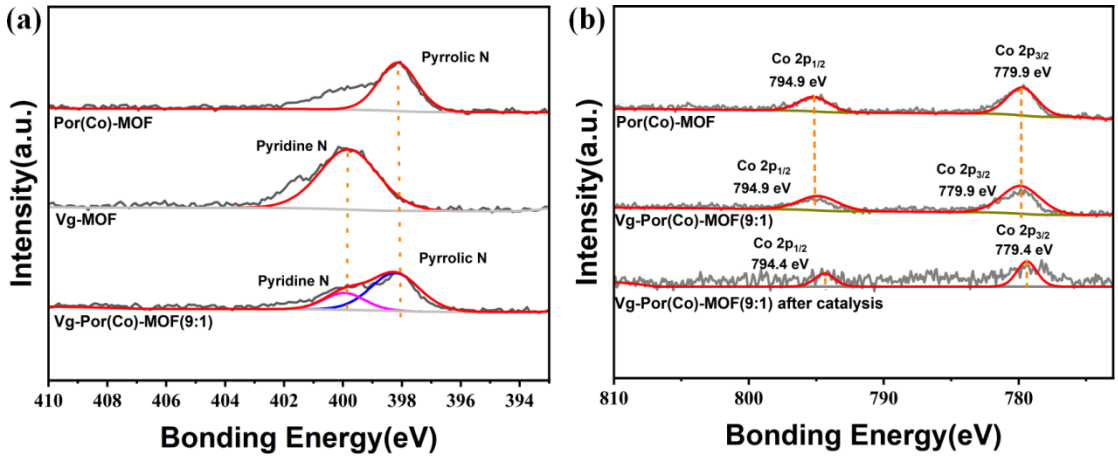

Figure S12. High-resolution XPS spectra of (a) N 1s for Por(Co)-MOF, Vg-MOF and Vg-Por(Co)-MOF(9:1), (b) Co 2p for Por(Co)-MOF, Vg-Por(Co)-MOF(9:1) and Vg-Por(Co)-MOF(9:1) after CO_2RR testing.

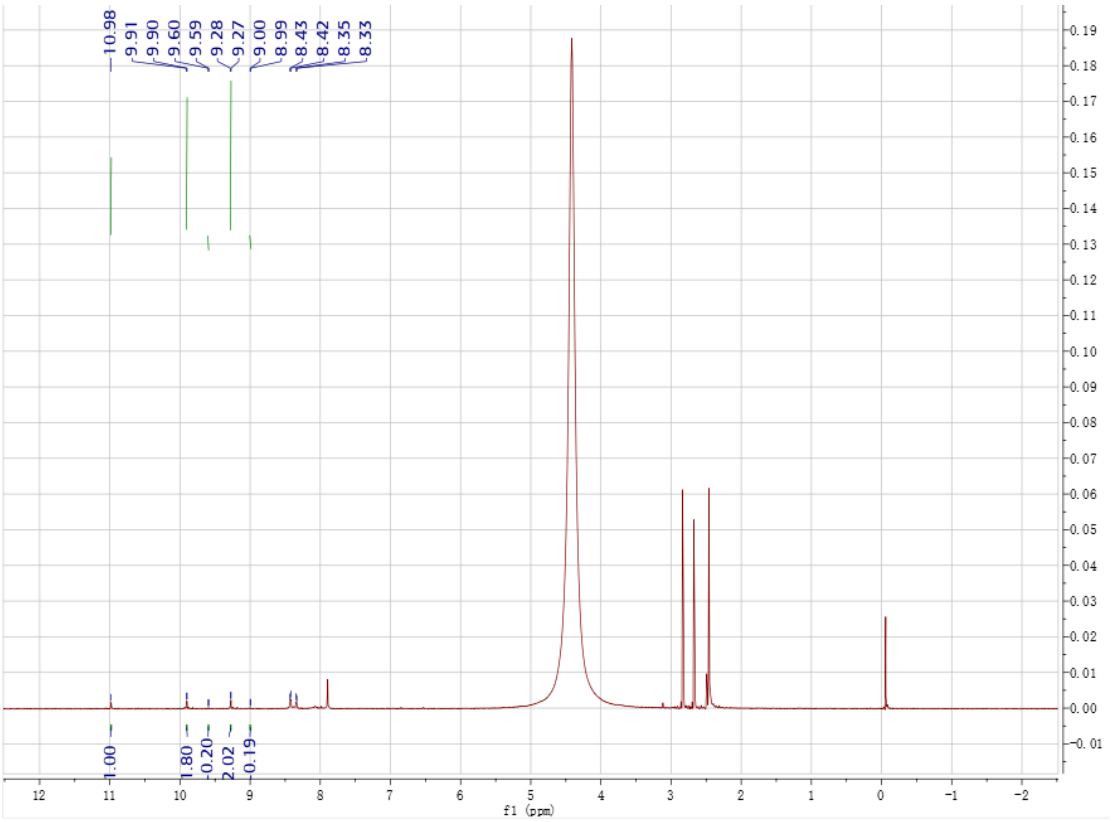

Figure S13. ^{1}H NMR spectrum of digested Vg-Por(Co)-MOF(9:1) sample in DMSO-d6 (HF) (r.t).

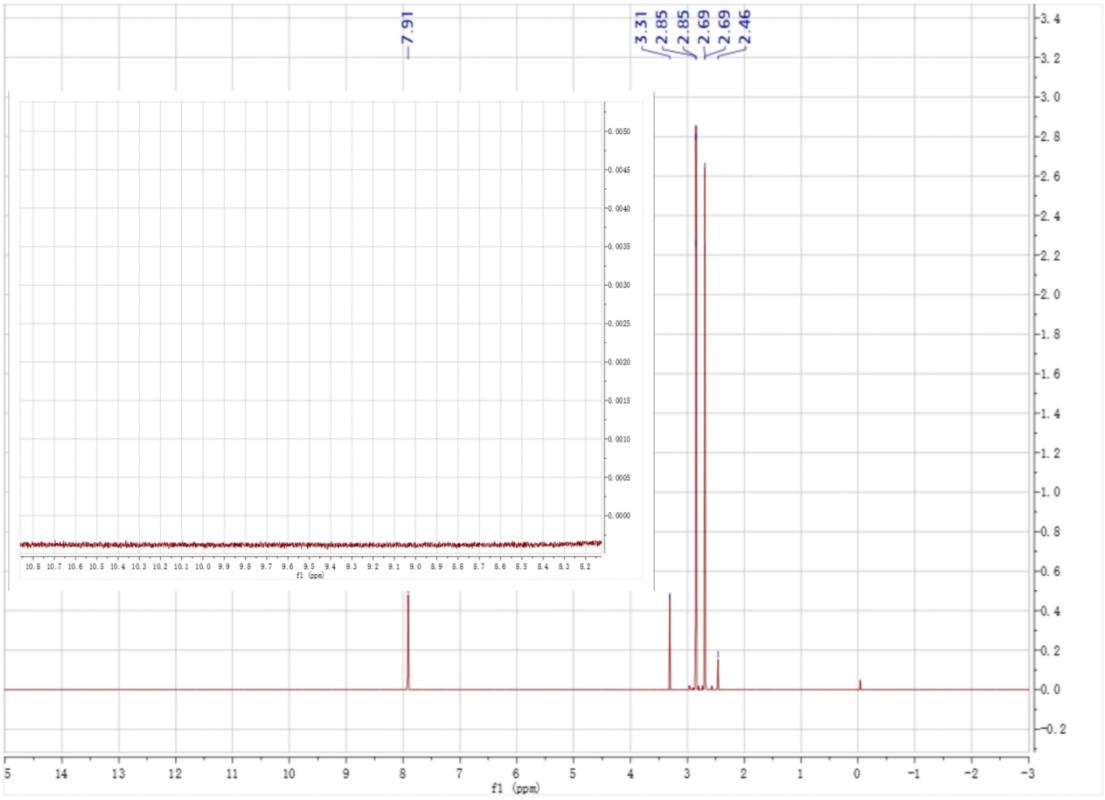

Figure S14. ^{1}H NMR spectrum of solvent Vg-Por(Co)-MOF(9:1) was extracted with DMF by Soxhlet extractor.

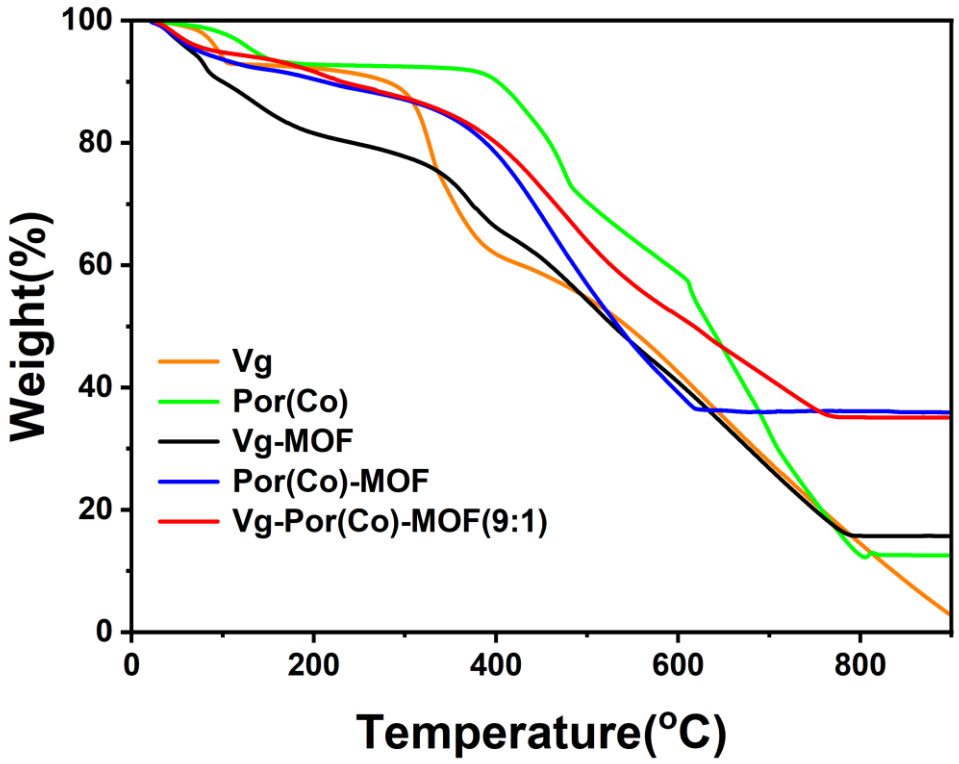

Figure S15. Thermogravimetric analysis of Vg, Por(Co), Vg-MOF, Por(Co)-MOF and Vg-Por(Co)-MOF(9:1).

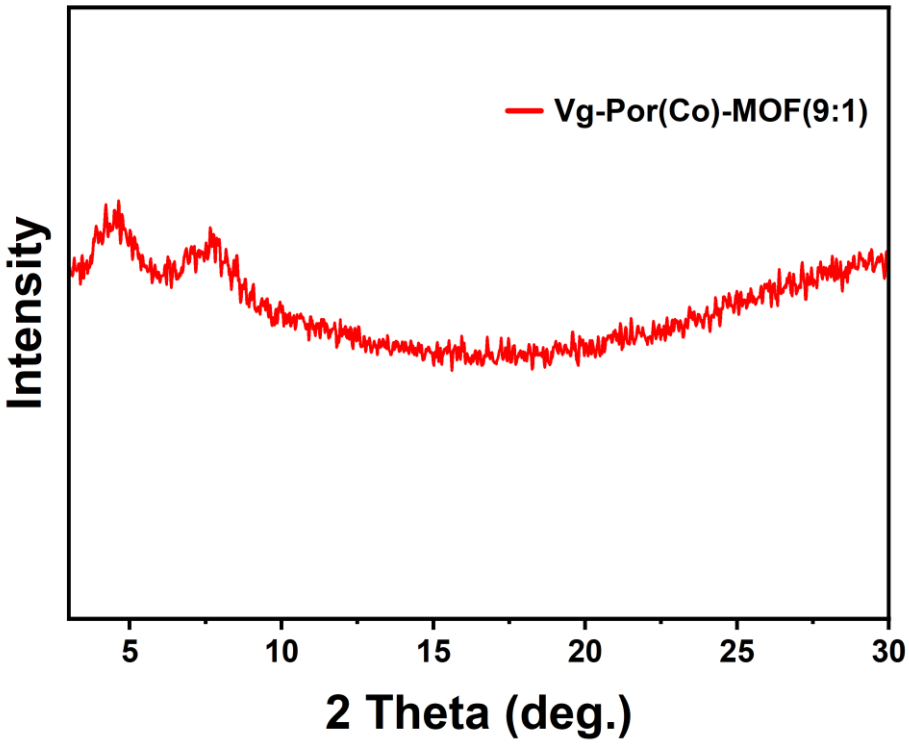

Figure S16. PXRD patterns of Vg-Por(Co)-MOF(9:1) after CO_2RR test.

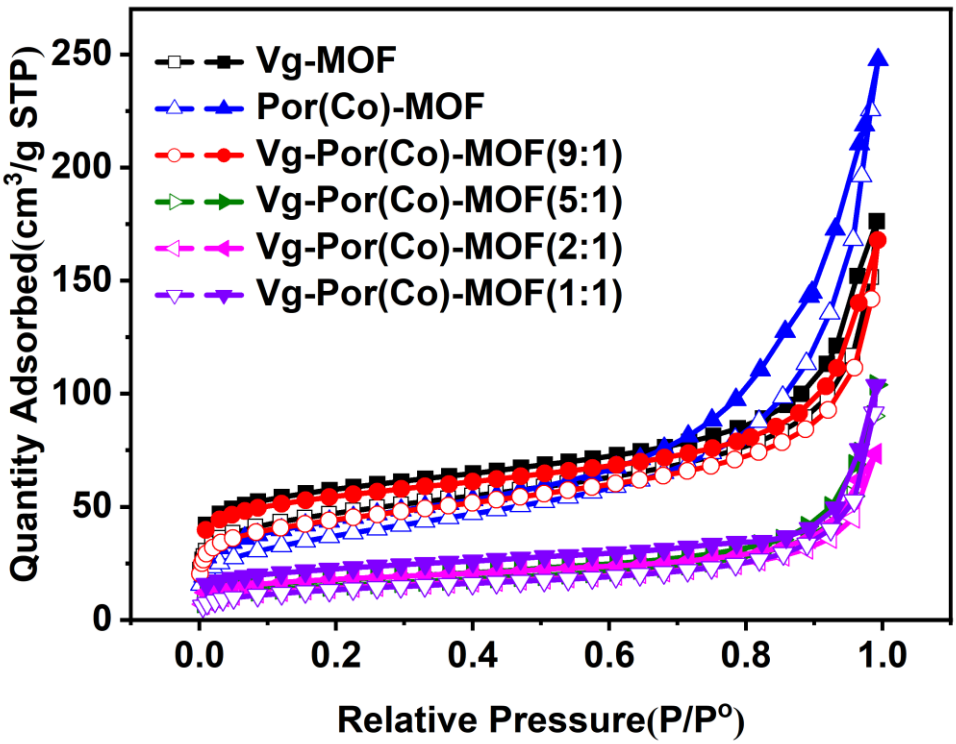

Figure S17. Nitrogen physisorption isotherms at 77 K for Vg-MOF, Por(Co)-MOF, Vg-Por(Co)-MOF(1:1), Vg-Por(Co)-MOF(2:1), Vg-Por(Co)-MOF(5:1) and Vg-Por(Co)-

MOF(9:1).

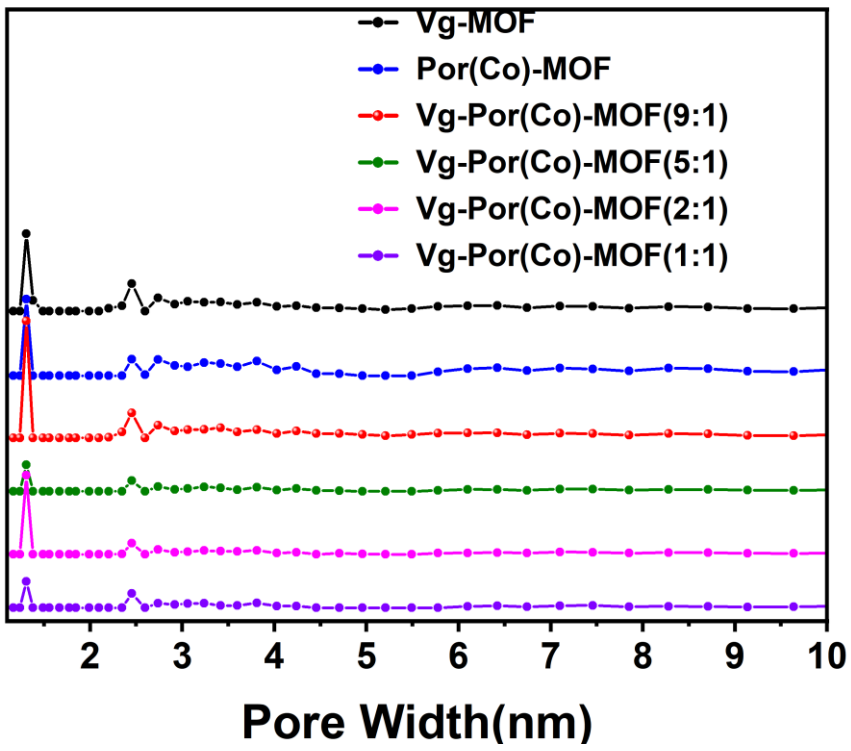

Figure S18. The pore-size distribution profile of Vg-MOF, Por(Co)-MOF, Vg-Por(Co)-MOF(1:1), Vg-Por(Co)-MOF(2:1), Vg-Por(Co)-MOF(5:1) and Vg-Por(Co)-MOF(9:1).

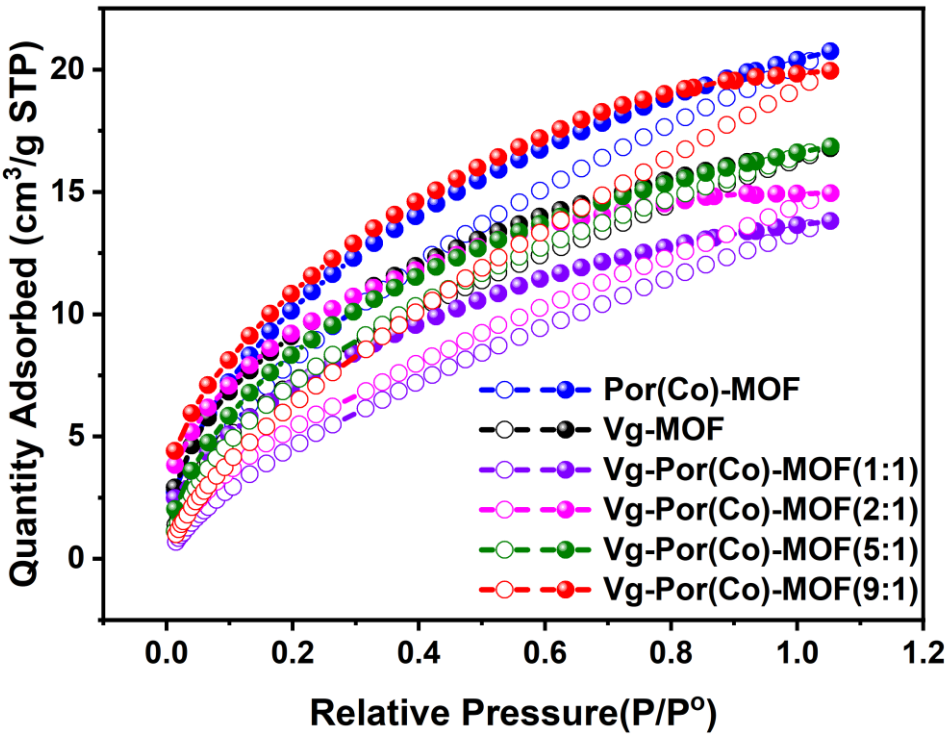

Figure S19. CO_2 adsorption curves of Vg-MOF, Por(Co)-MOF, Vg-Por(Co)-MOF(1:1), Vg-Por(Co)-MOF(2:1), Vg-Por(Co)-MOF(5:1) and Vg-Por(Co)-MOF(9:1) at 293 K.

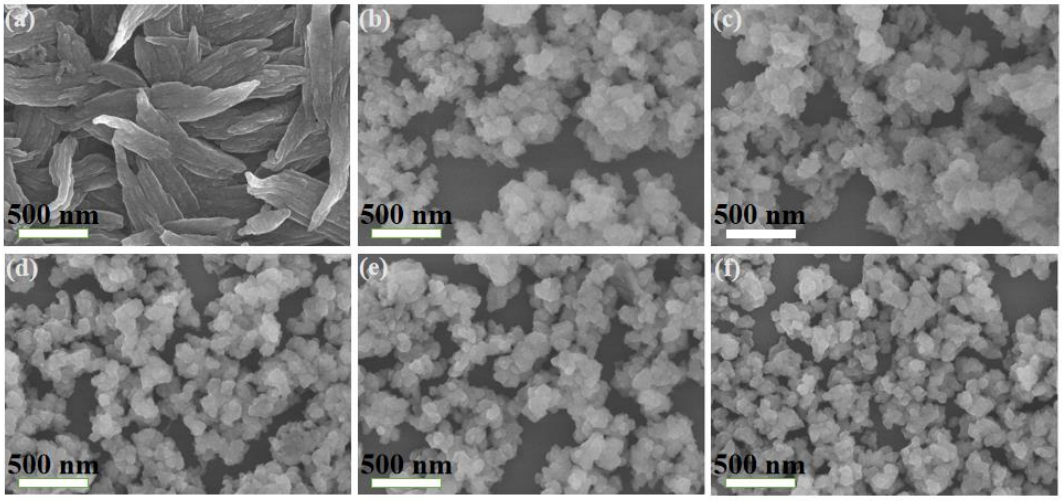

Figure S20. SEM images of (a) Vg-MOF, (b) Por(Co)-MOF, (c) Vg-Por(Co)-MOF(1:1), (d) Vg-Por(Co)-MOF(2:1), (e) Vg-Por(Co)-MOF(5:1)and (f) Vg-Por(Co)-MOF(9:1) with scale bar 500 nm.

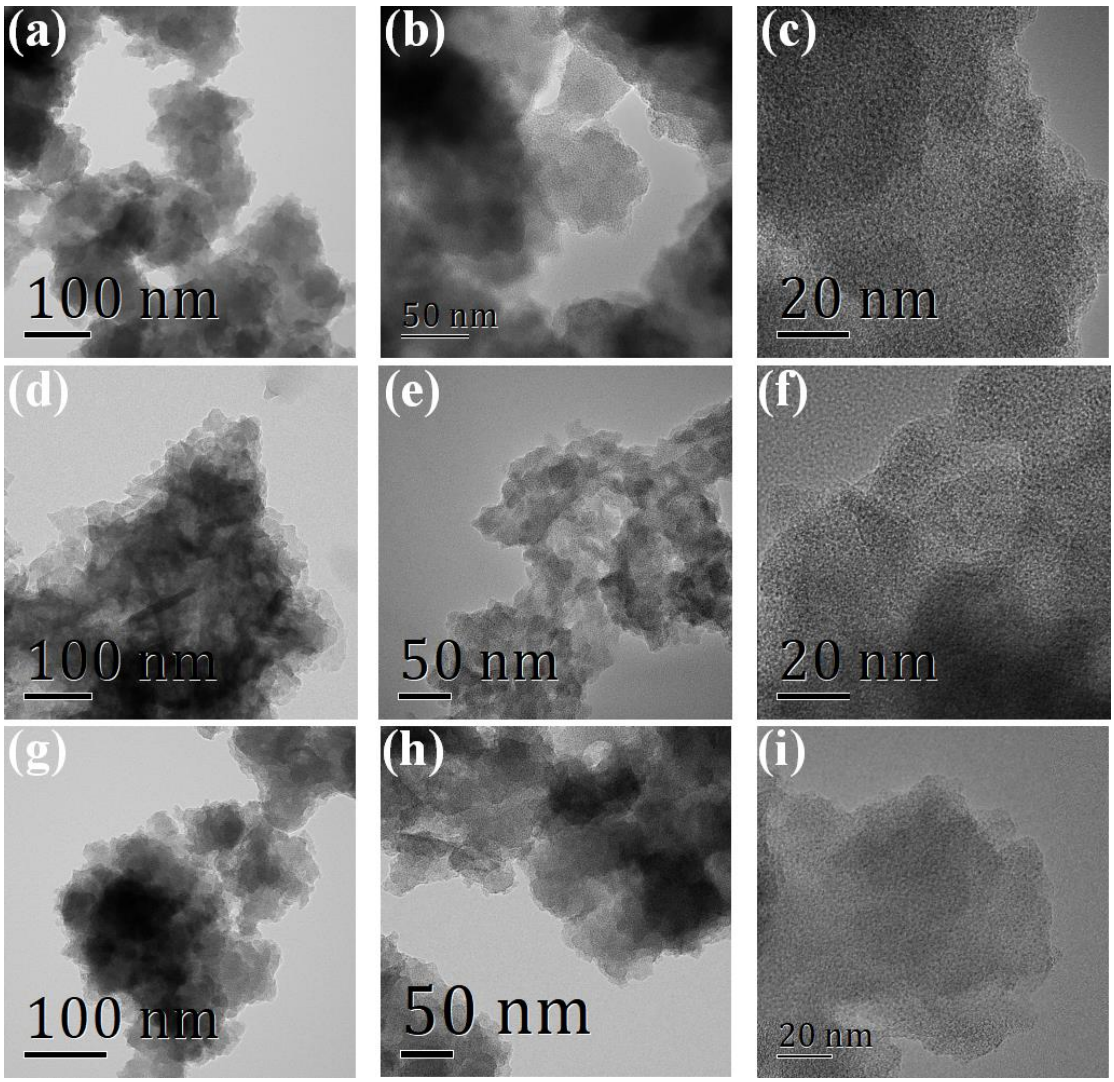

Figure S21. TEM image of Por(Co)-MOF nanosheets (a) 100 nm (b) 50 nm(c) 20 nm, Vg-MOF nanosheets (d) 100 nm (e) 50nm (f) 20nm and Vg-Por(Co)-MOF(9:1) (g) 100 nm (h) 50 nm (i) 20nm.

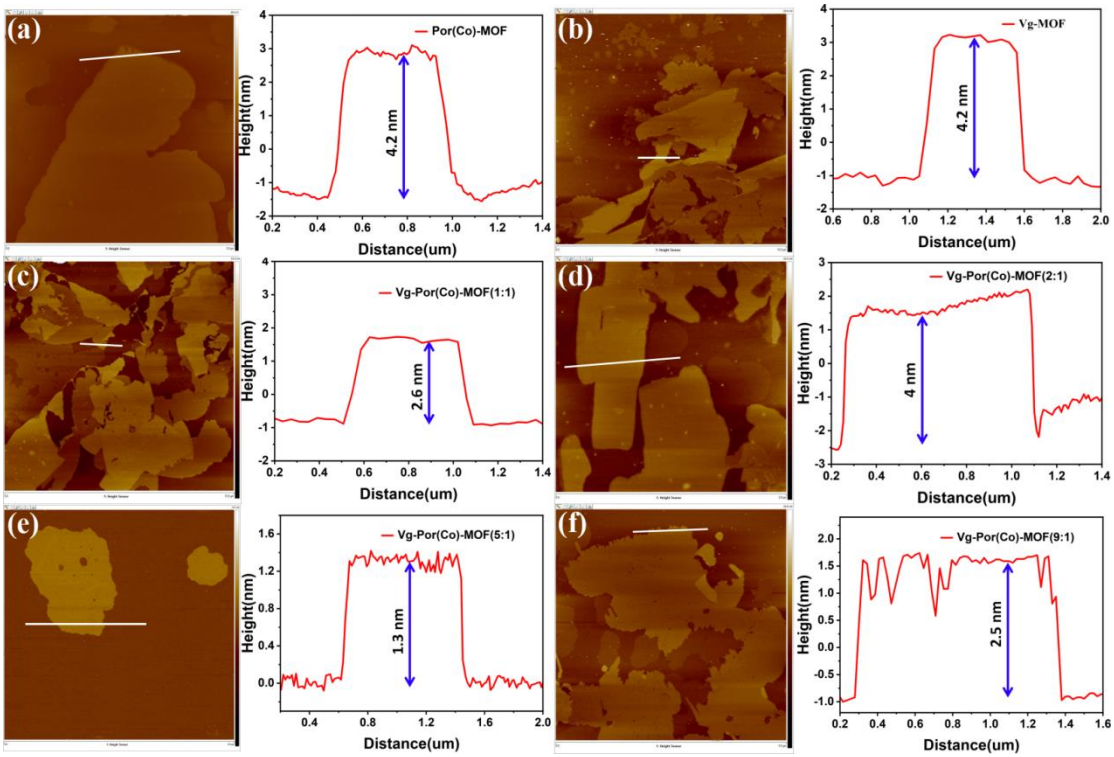

Figure S22. AFM image and the corresponding crosssectional profile of (a) Vg-MOF, (b) Por(Co)-MOF, (c) Vg-Por(Co)-MOF(1:1), (d) Vg-Por(Co)-MOF(2:1), (e) Vg-Por(Co)-MOF(5:1)and (f) Vg-Por(Co)-MOF(9:1) nanosheets (color online).

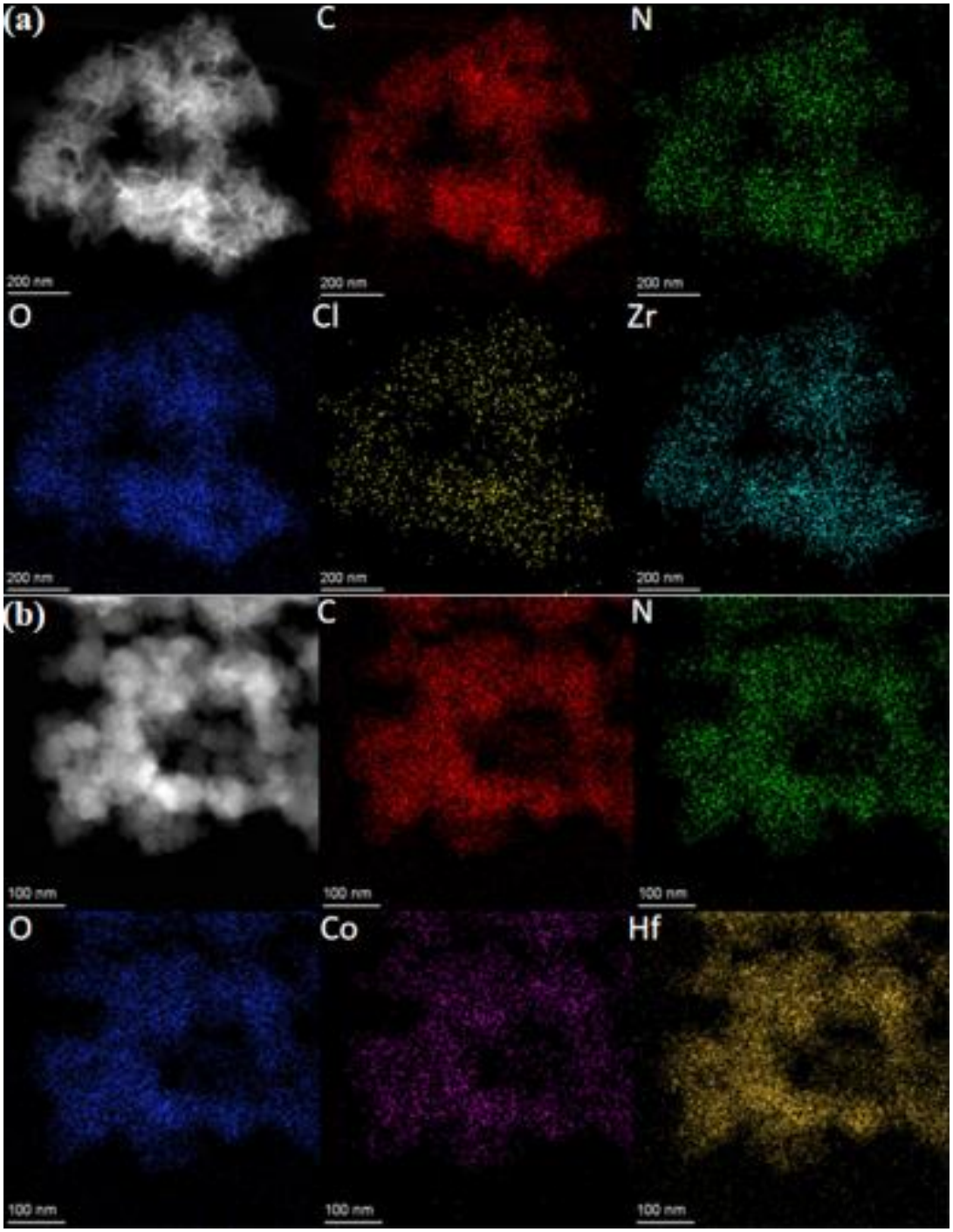

Figure S23. HAADF-STEM image of (a) Vg-MOF and EDS mapping of C, N, O, Cl and Zr elements(color online) and (b) Por(Co)-MOF and EDS mapping of C, N, O, Co, and Hf elements (color online).

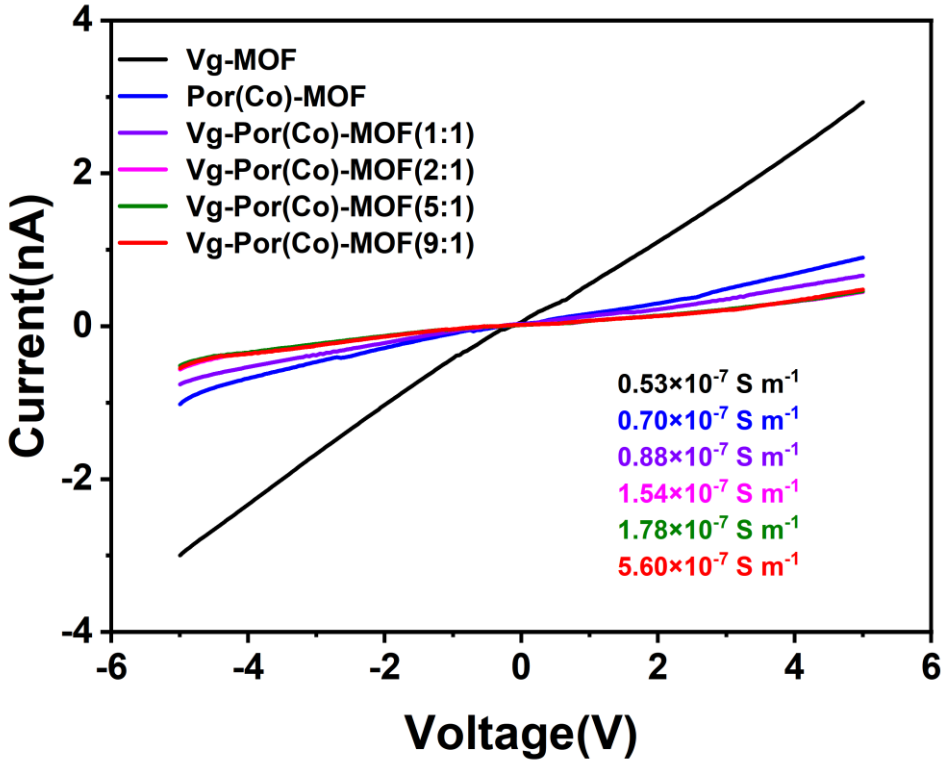

Figure S24. Current-voltage characteristic of Vg-MOF, Por(Co)-MOF and Vg-Por(Co)-MOF(n:1) (n = 1, 2, 5, 9) using the two-contact probe method.

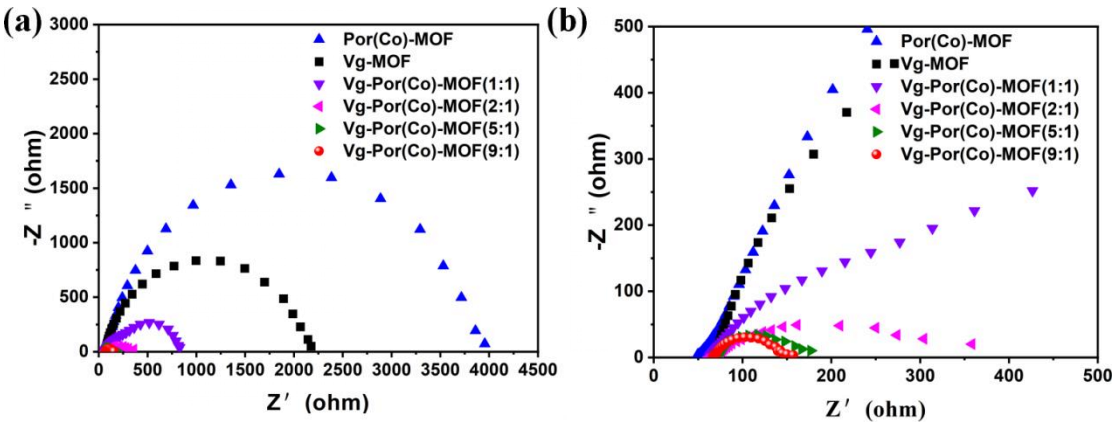

Figure S25. (a) Nyquist plots of Vg-MOF, Por(Co)-MOF, Vg-Por(Co)-MOF(1:1), Vg-Por(Co)-MOF(2:1), Vg-Por(Co)-MOF(5:1) and Vg-Por(Co)-MOF(9:1) in 0.2 M Na_2SO_4. (b) an enlarged image of (a).

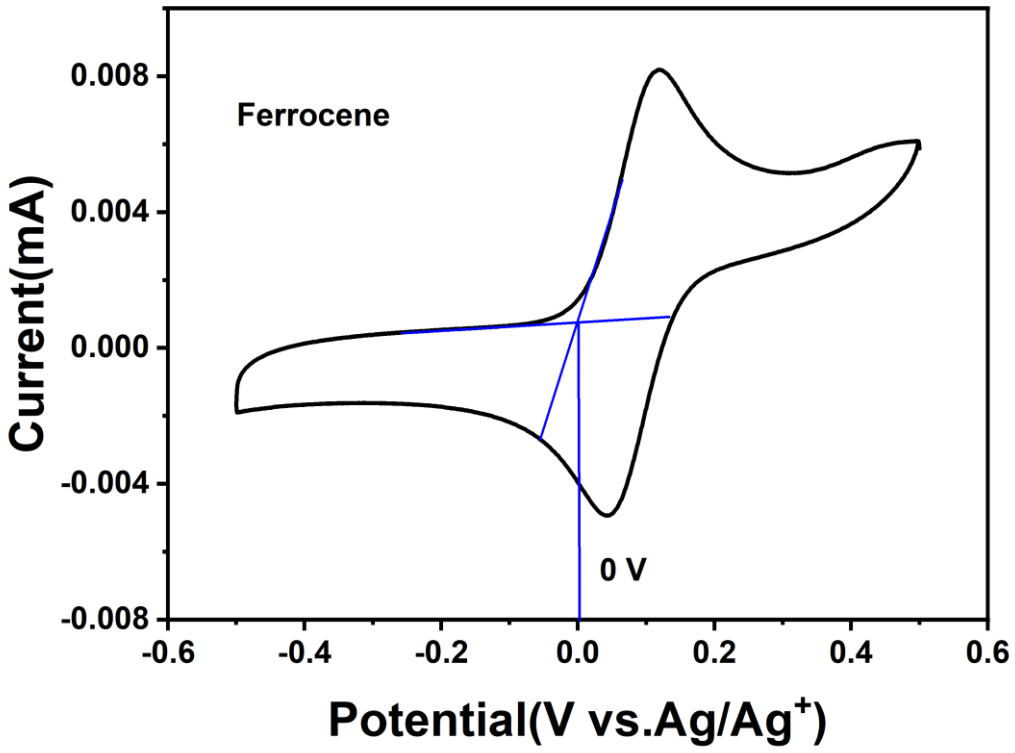

Figure S26. Cyclic voltammograms of ferrocene (internal standard) in 0.1 M nBu_4NPF_6 in DMF at room temperature ($E(Fc/Fc^+) = 0$ V).

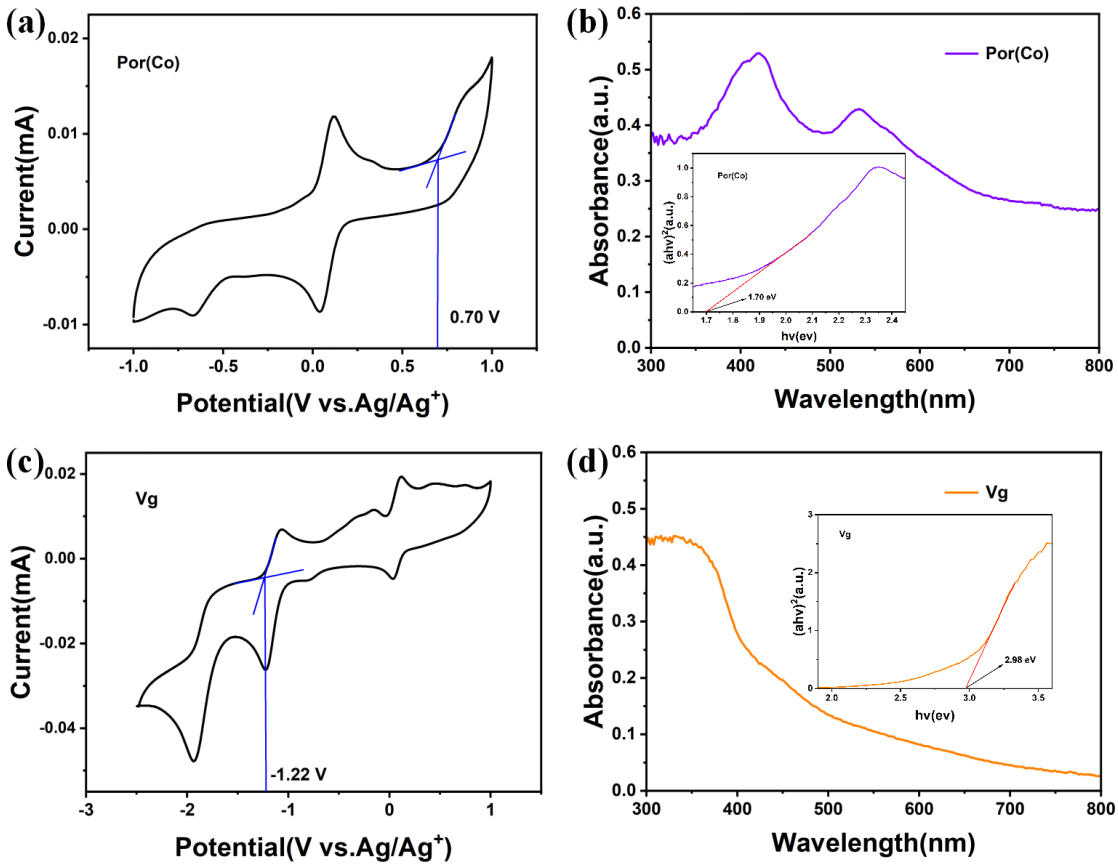

Figure S27. The cyclic voltammogram and optical tests of Por(Co) and Vg. (a) Cyclic voltammograms of Por(Co). (b) Solid state UV of Por(Co) (inset Tauc plot). (c) Cyclic voltammograms of Vg. (d) Solid state UV of Vg (inset Tauc plot).

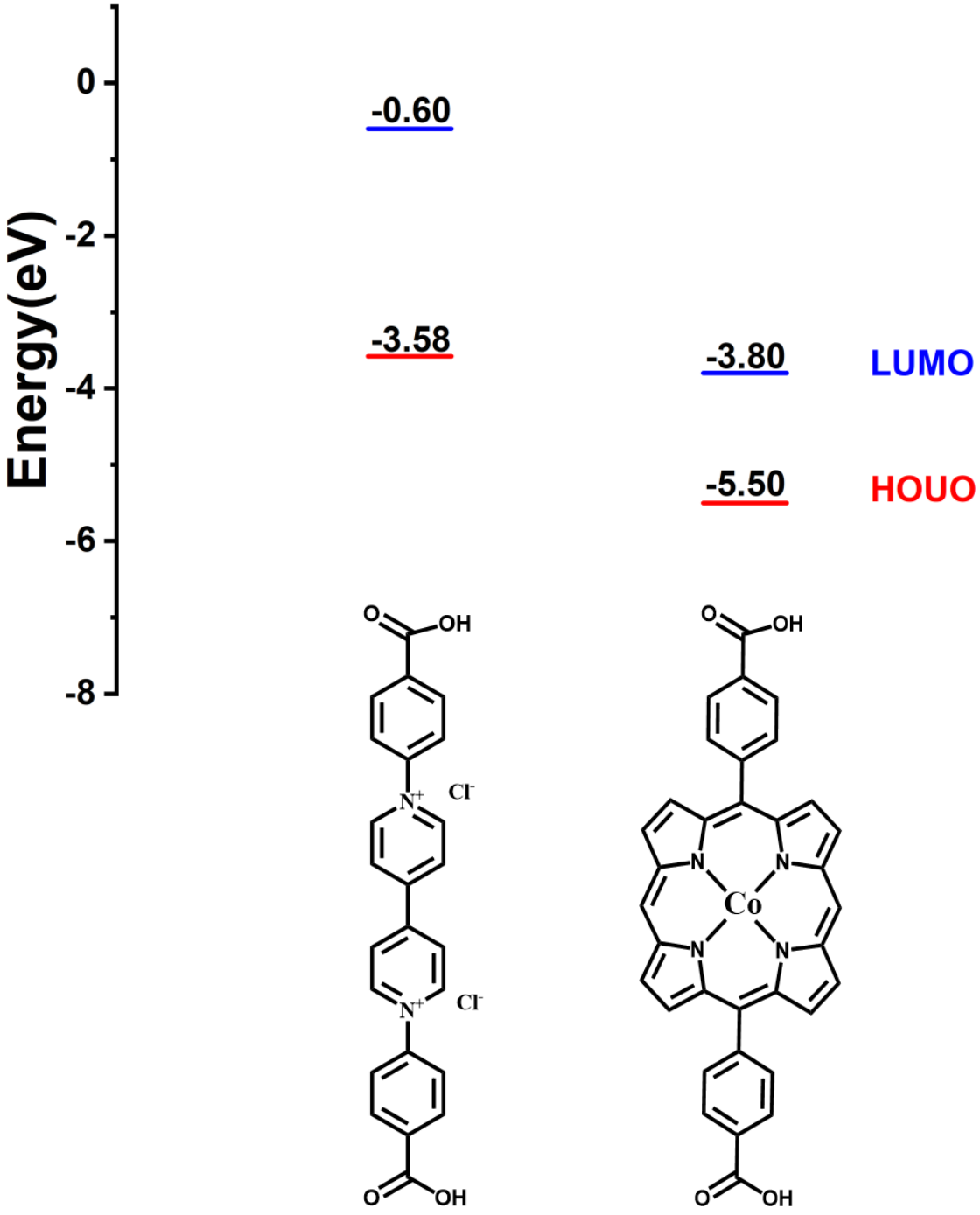

Figure S28. Relevant energy levels of the monomers with HOMO (red) and LUMO (blue), which were determined by combining CV measurements and UV-vis data.

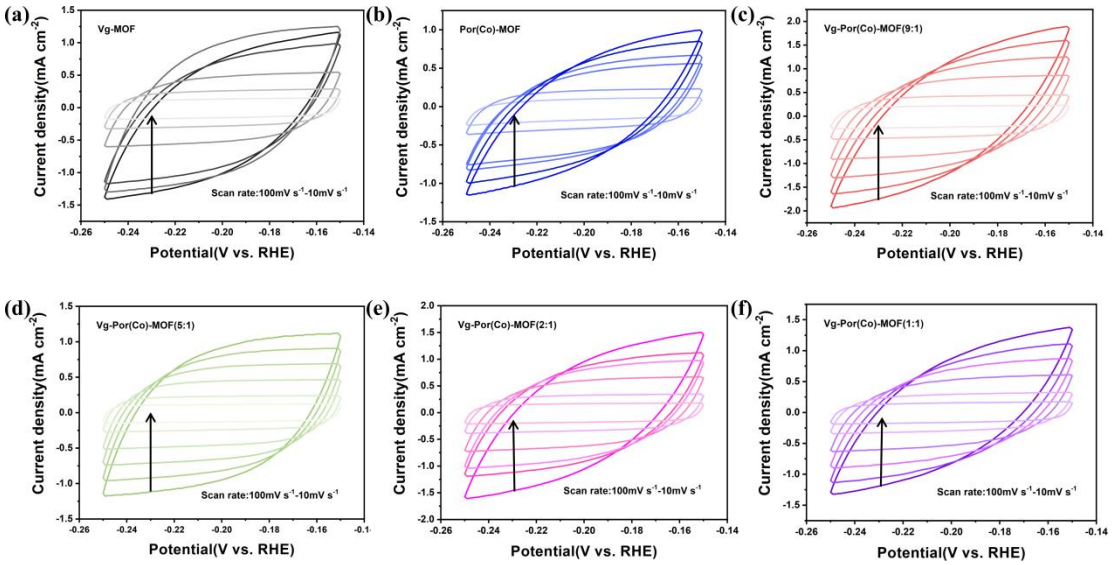

Figure S29. CV curves of Vg-MOF, Por(Co)-MOF, Vg-Por(Co)-MOF(1:1), Vg-Por(Co)-MOF(2:1), Vg-Por(Co)-MOF(5:1) and Vg-Por(Co)-MOF(9:1) in 0.5 M $KHCO_3$ solution.

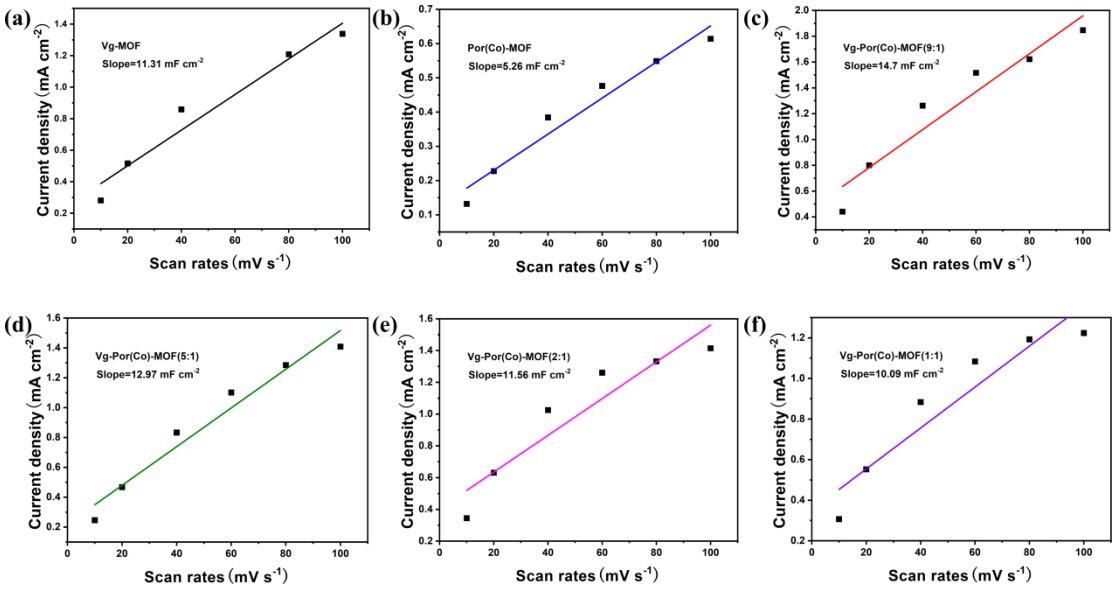

Figure S30. the current density differences vs. scan rates and corresponding yielded Cdl for Vg-MOF, Por(Co)-MOF, Vg-Por(Co)-MOF(1:1), Vg-Por(Co)-MOF(2:1), Vg-Por(Co)-MOF(5:1) and Vg-Por(Co)-MOF(9:1) in 0.5 M $KHCO_3$ electrolyte (color online).

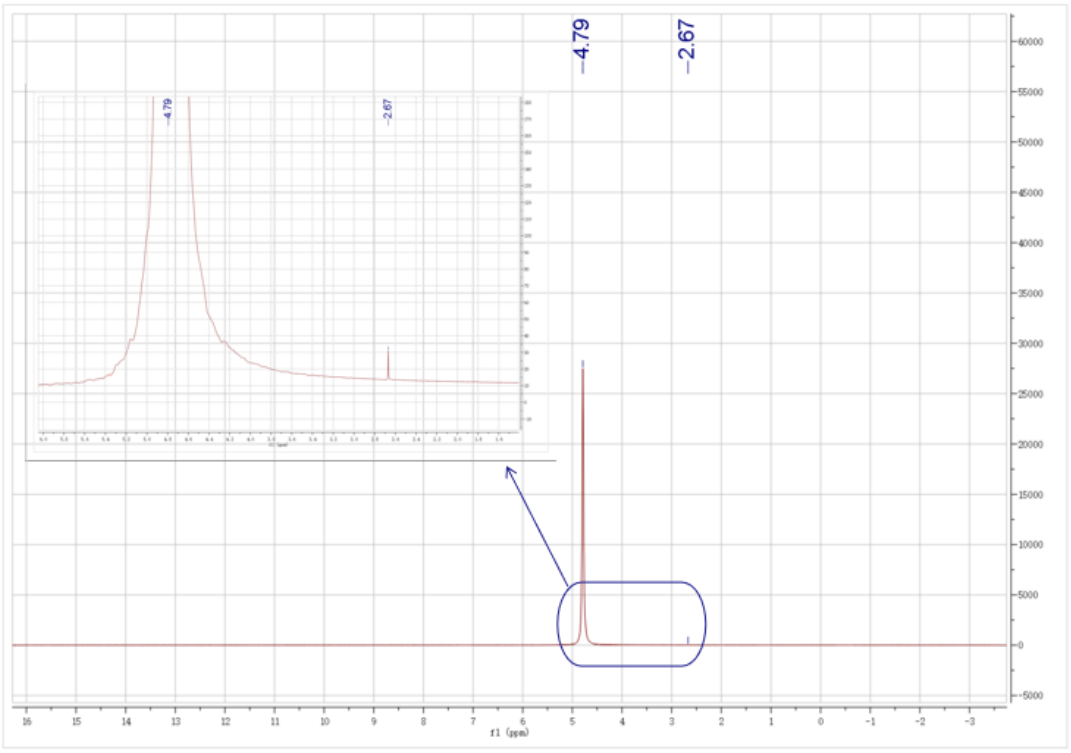

Figure S31. ^{1}HNMR spectrum of the electrolyte for Vg-Por(Co)-MOF(9:1) after CO_2RR testing.

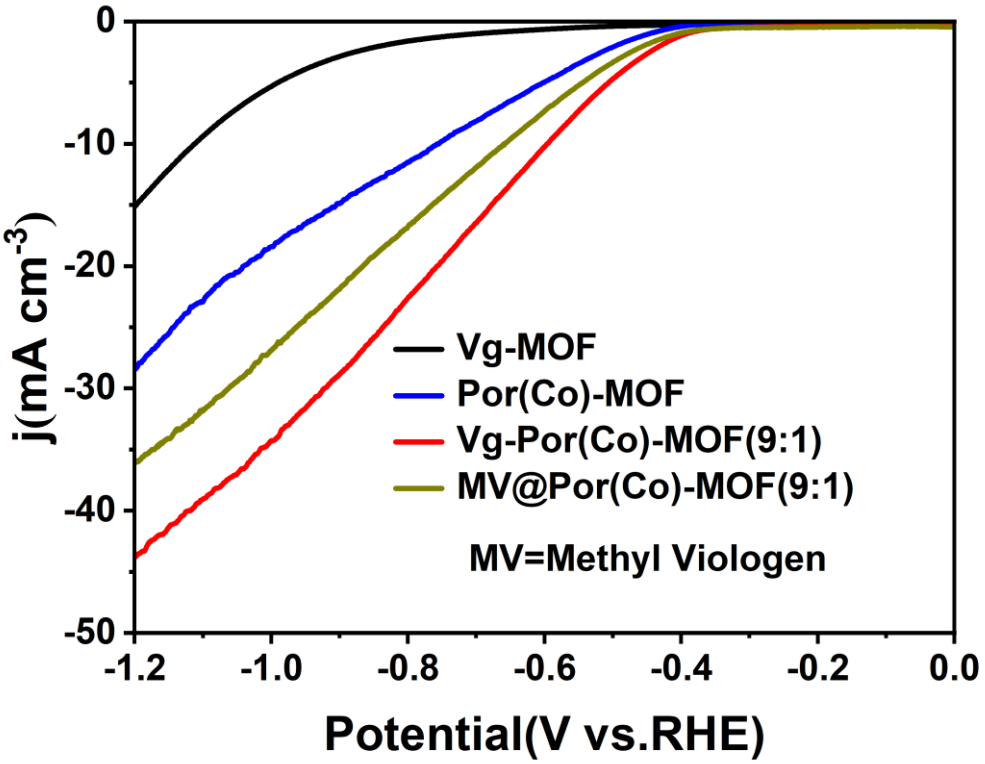

Figure S32. Electrocatalytic CO_2RR performance in a H-type cell system. LSV curves

of Vg-MOF, Por(Co)-MOF, Vg-Por(Co)-MOF(9:1) and MV@Por(Co)-MOF(9:1) (Me = Methyl Viologen) in 0.5 M $KHCO_3$ electrolyte under CO_2.

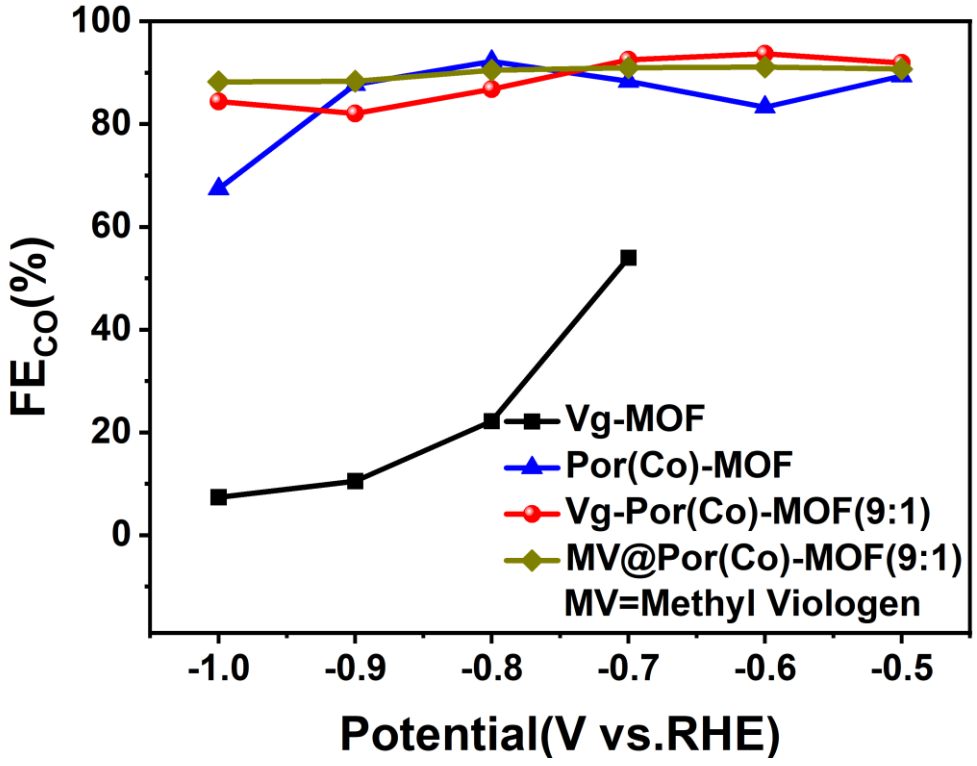

Figure S33. Electrocatalytic CO_2RR performance in a H-type cell system. Faradaic efficiencies for Vg-MOF, Por(Co)-MOF, Vg-Por(Co)-MOF(9:1) and MV@Por(Co)-MOF(9:1) (Me=Methyl Viologen).

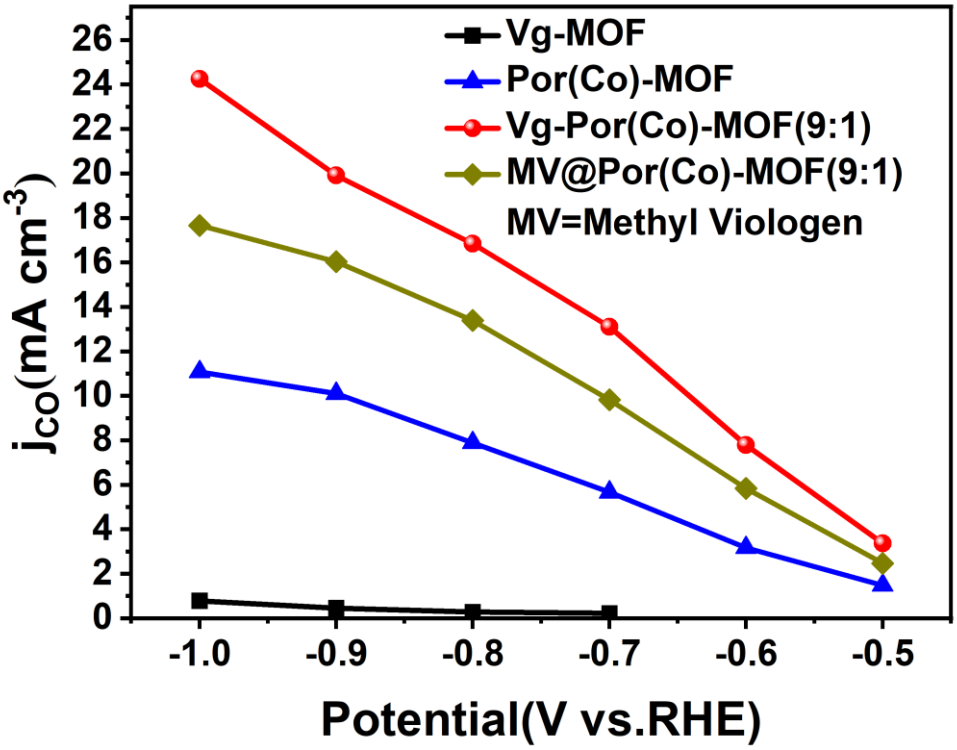

Figure S34. Electrocatalytic CO_2RR performance in a H-type cell system. Partial current density of CO for Vg-MOF, Por(Co)-MOF, Vg-Por(Co)-MOF(9:1) and MV@Por(Co)-MOF(9:1) (Me=Methyl Viologen).

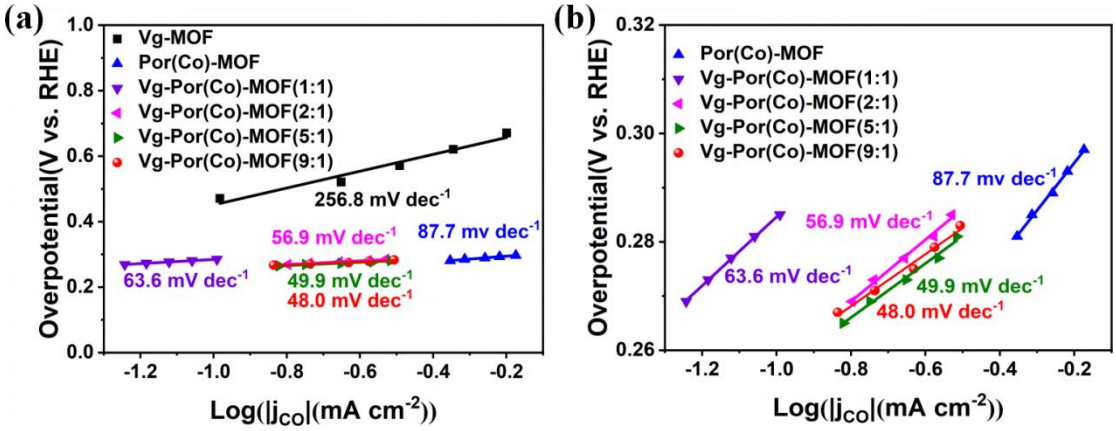

Figure S35. Tafel plots of Vg-MOF, Por(Co)-MOF, Vg-Por(Co)-MOF(1:1), Vg-Por(Co)-MOF(2:1), Vg-Por(Co)-MOF(5:1) and Vg-Por(Co)-MOF(9:1) in 0.5 M $KHCO_3$. (b) an enlarged image of (a).

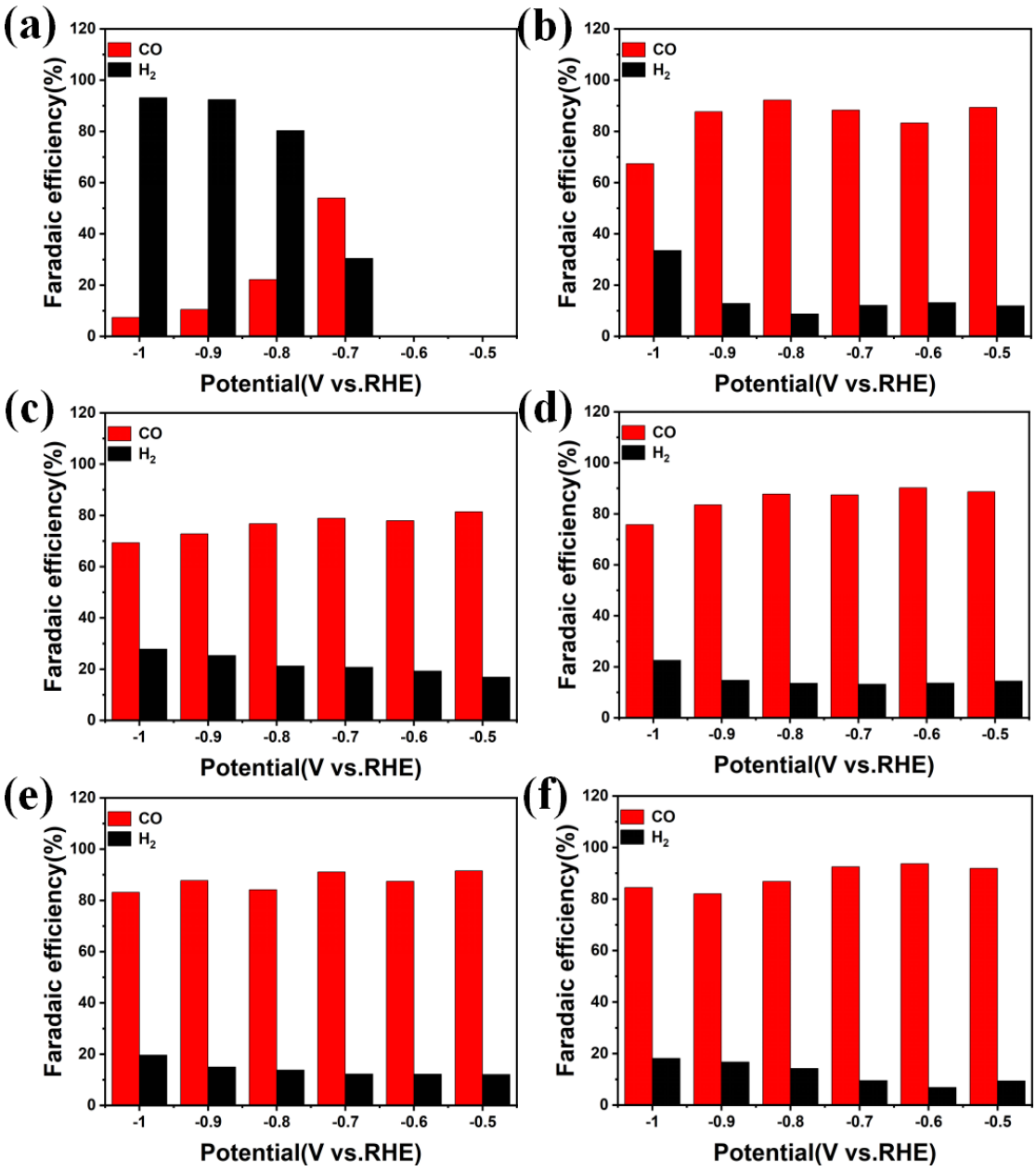

Figure S36. Electrocatalytic CO_2RR performance in a H-type cell system. FE_{CO} from -0.5 V to -1.0 V vs. RHE of Vg-MOF (a), Por(Co)-MOF (b), Vg-Por(Co)-MOF(1:1) (c), Vg-Por(Co)-MOF(2:1) (d), Vg-Por(Co)-MOF(5:1) (e) and Vg-Por(Co)-MOF(9:1) (f).

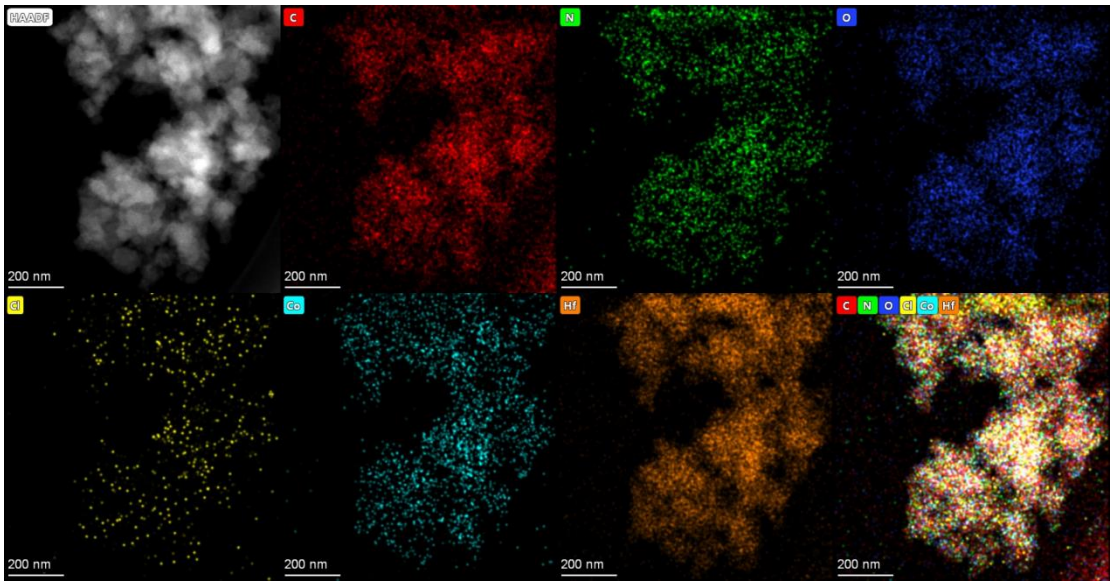

Figure S37. HAADF-STEM image, and corresponding elemental mapping showing the distribution of C, N, O, Cl, Co and Hf of Vg-Por(Co)-MOF(9:1) after CO_2RR text, respectively.

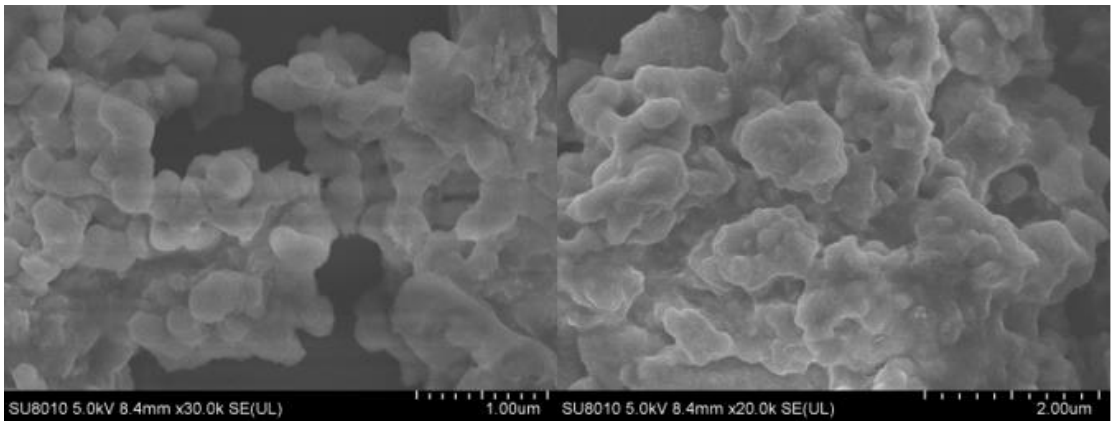

Figure S38. SEM image of Vg-Por(Co)-MOF(9:1) after CO_2RR text.

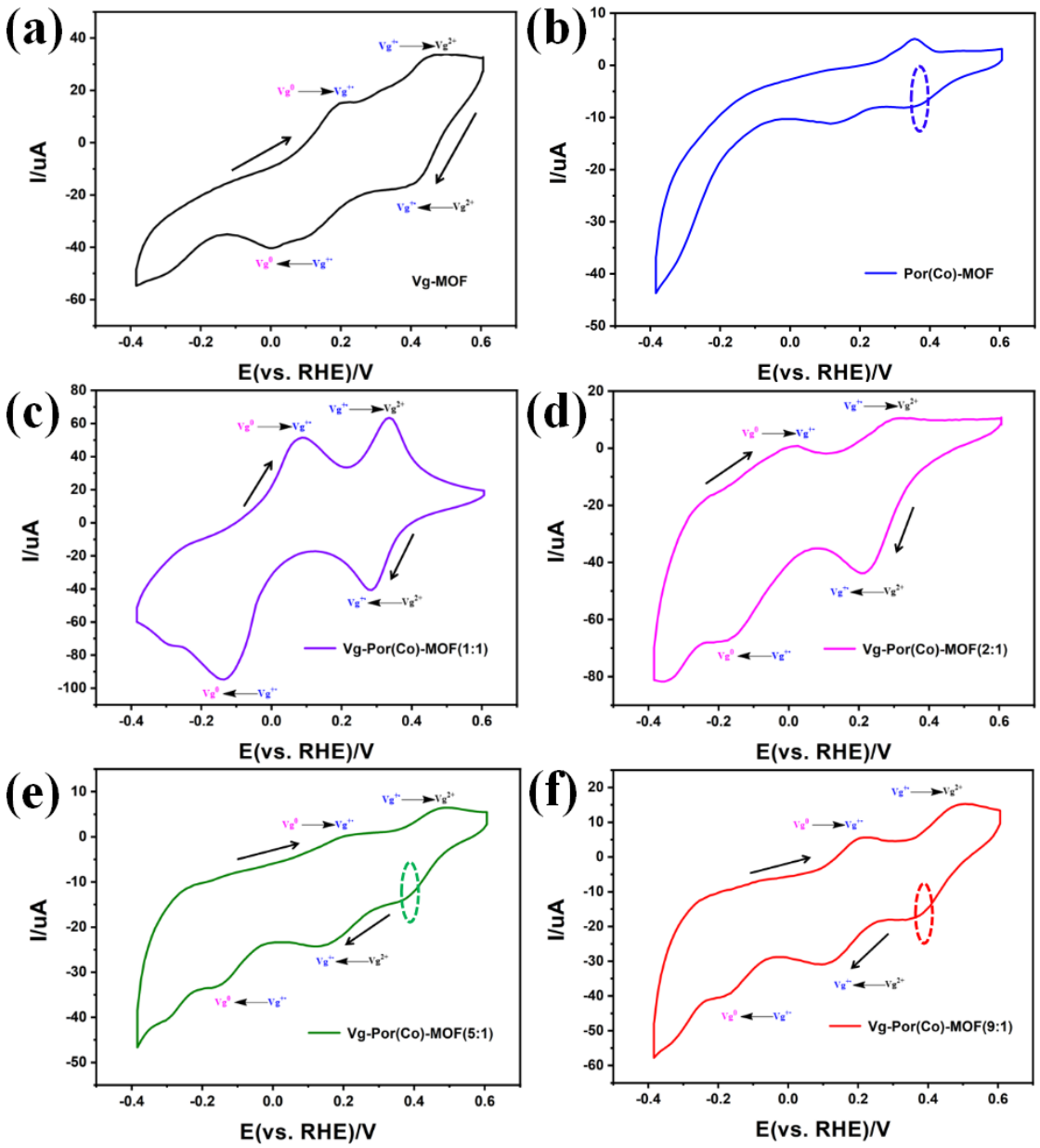

Figure S39. The cyclic voltammogram of Vg-MOF, Por(Co)-MOF, Vg-Por(Co)-MOF(1:1), Vg-Por(Co)-MOF(2:1), Vg-Por(Co)-MOF(2:1), Vg-Por(Co)-MOF(5:1) and Vg-Por(Co)-MOF(9:1) in 0.2 M Na_2SO_4 electrolyte under N_2 (In the circle is a reduction peak of Por(Co)-MOF).

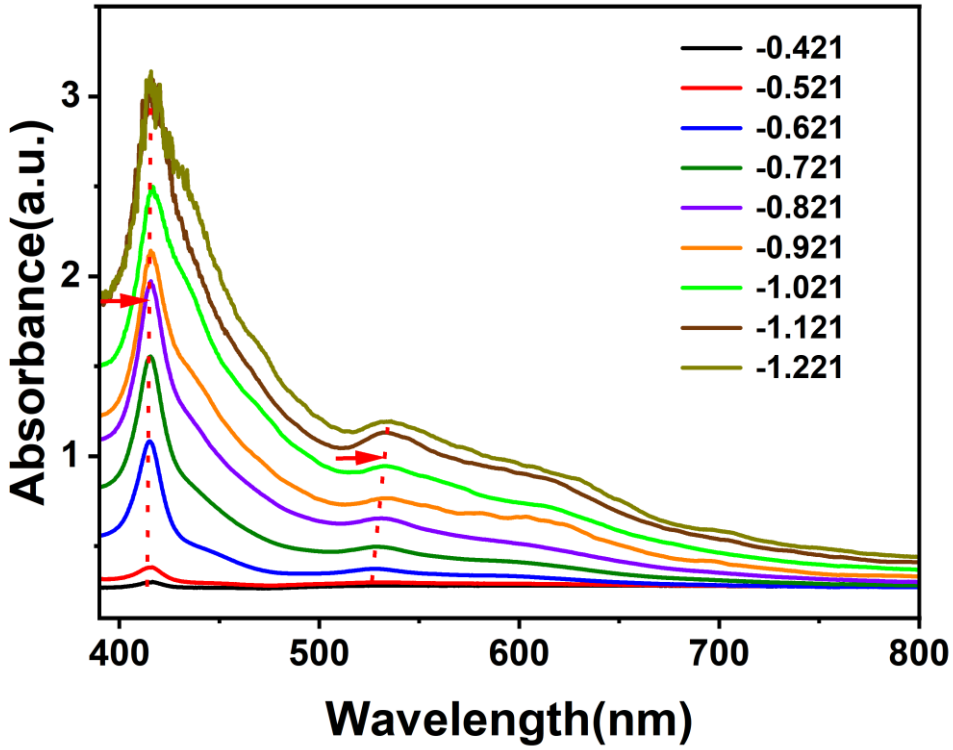

Figure S40. Spectroelectrochemistry of Vg-Por(Co)-MOF(9:1) for electrochemical reduction carried out in 0.2 M Na_2SO_4 from −0.421 to −1.221 V in intervals of 0.1 V.

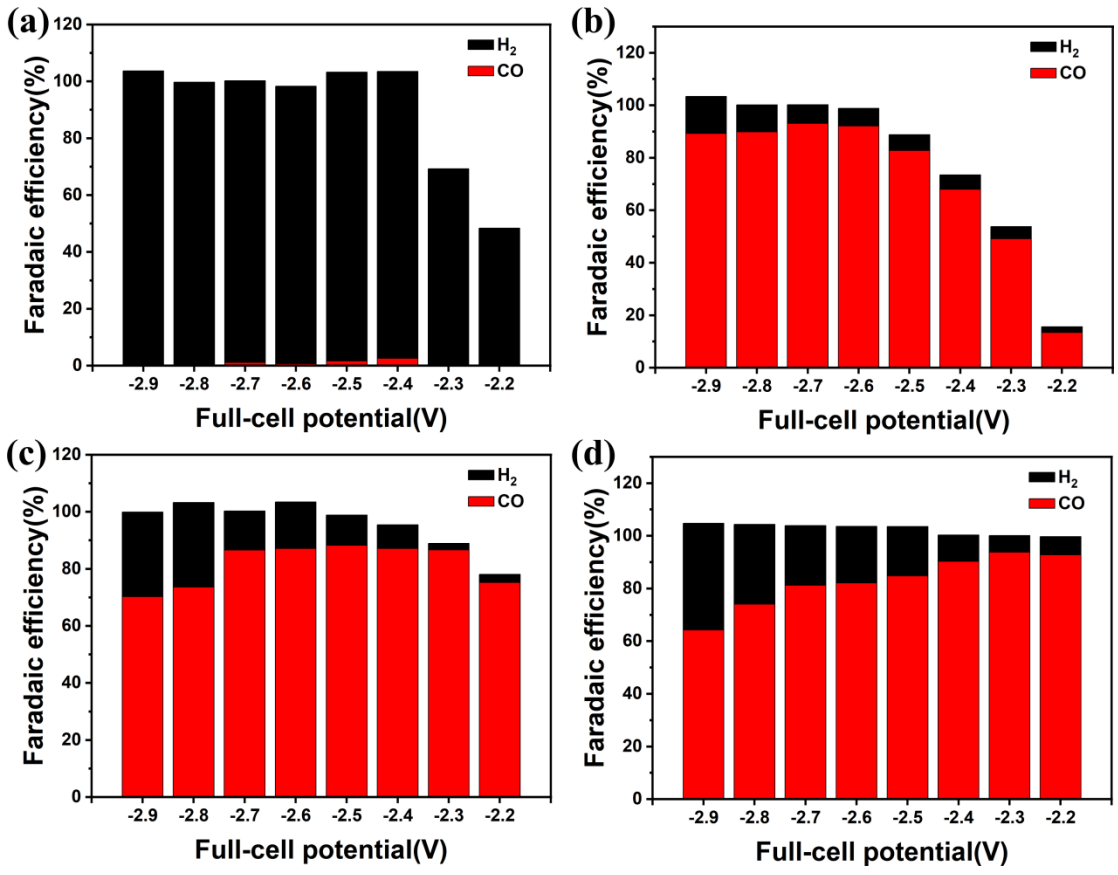

Figure S41. Electrocatalytic CO_2RR performance in MEA system. FE_{CO} from 2.2 V to 2.9 V of Vg-MOF (a), Por(Co)-MOF (b), Vg-Por(Co)-MOF(1:1) (c) and Vg-Por(Co)-MOF(9:1) (d).

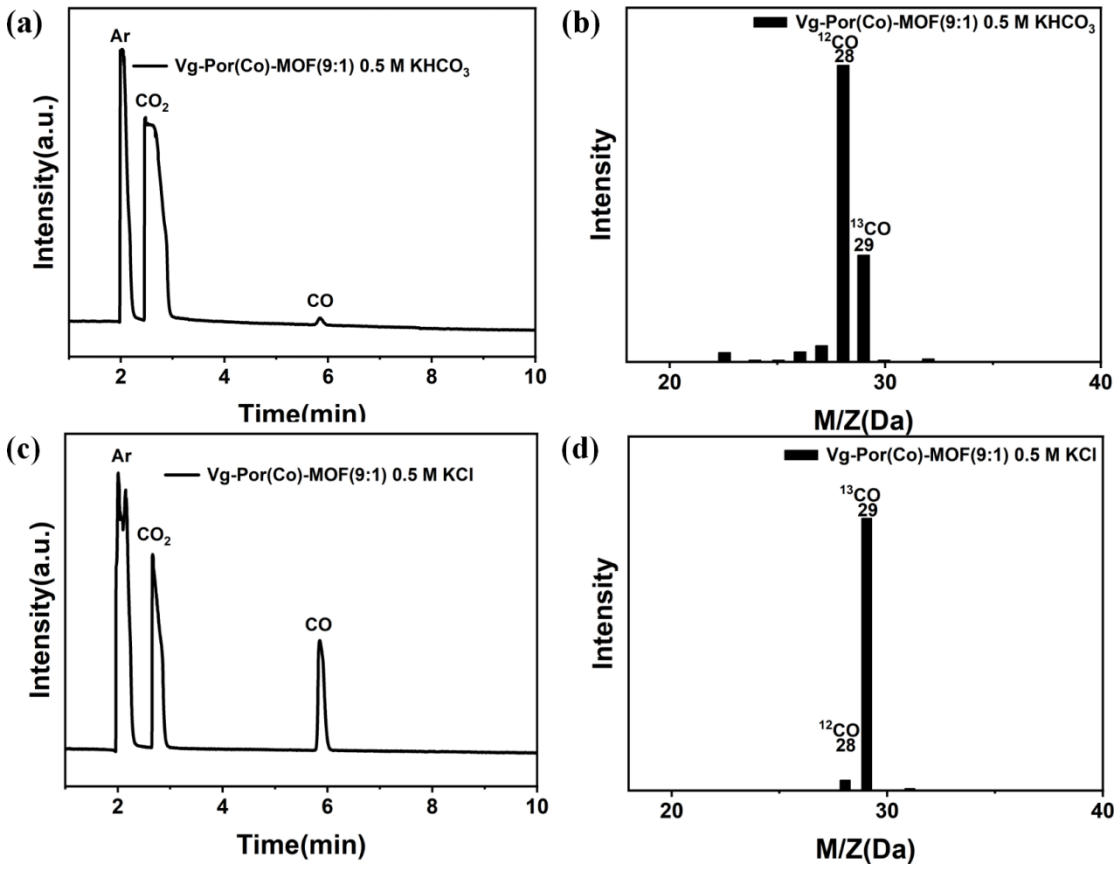

Figure S42. (a) The gas chromatography and (b) Mass spectrometry of Vg-Por(Co)-MOF(9:1) text in 0.5 M $KHCO_3$. (c) The gas chromatography and (d) Mass spectrometry of Vg-Por(Co)-MOF(9:1) text in 0.5 M KCl.

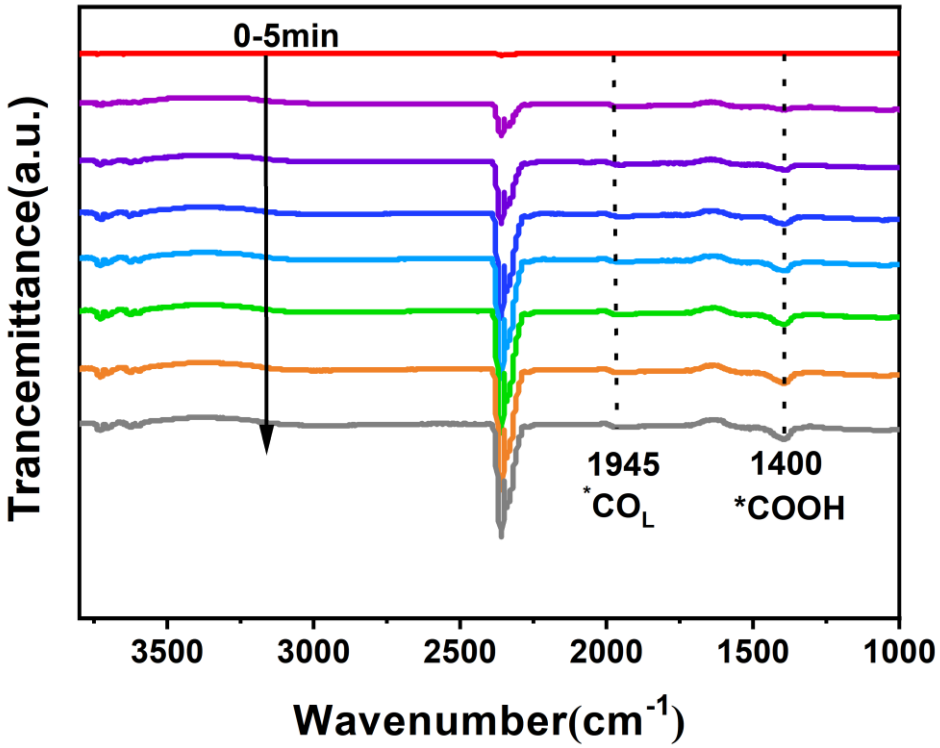

Figure S43. Insitu ATR-IR of Vg-Por(Co)-MOF(9:1) at -0.6 V.

Table S1. ICP and EA results of Co, C, N, O and H in Vg-MOF, Por(Co)-MOF and Vg-Por(Co)-MOF(n:1) (n = 1, 2, 5, 9).

Sample	**Co**	**C**	**N**	**O**	**H**
Vg-MOF		31.70%	4.66%		3.89%
Por(Co)-MOF	2.75%	38.98%	7.44%	14.78%	3.62%
Vg-Por(Co)-MOF(1:1)	1.60%	38.07%	6.47%	17.72%	3.72%
Vg-Por(Co)-MOF(2:1)	2.14%	37.78%	6.65%	16.60%	3.71%
Vg-Por(Co)-MOF(5:1)	2.30%	39.12%	7.14%	16.75%	3.74%
Vg-Por(Co)-MOF(9:1)	2.67%	39.78%	7.26%	15.78%	3.66%

Table S2. BET surface area and pore volume for Vg-MOF, Por(Co)-MOF, Vg-Por(Co)-MOF(n:1) (n = 1, 2, 5, 9).

Sample	**BET(m^2/g)**	**Pore volume(m^3/g)**
Vg-MOF	118.1	1.29
Por(Co)-MOF	165.8	1.29
Vg-Por(Co)-MOF(1:1)	43.1	1.29
Vg-Por(Co)-MOF(2:1)	48.1	1.29
Vg-Por(Co)-MOF(5:1)	51.1	1.29
Vg-Por(Co)-MOF(9:1)	154.7	1.29

Table S3. CN, coordination number; R, distance between absorber and backscatter atoms; σ^2, Debye-Waller factor (a measure of thermal and static disorder in absorber-scatterer distances); R factor is used to value the goodness of the fitting.

Sample	**Path**	**CN**	**R(Å)**	**σ^2(10^{-3}Å^2)**	**R factor**
Vg-Por(Co)-MOF(9:1)	Co-N	4.11±0.64	1.967	2.10±4.82	0.03

Table S4. Comparison of CO partial current density of various catalysts electroreduction.

Catalyst	Electrolyte	Applied potential (V vs.RHE)	Partial current density of CO(mA cm^{-2})	Reference

Vg-Por(Co)-MOF(9:1)	0.5M $KHCO_3$	-1.0	24.3	This work
Vg-Por(Co)-MOF(9:1)	**1M KOH**	**2.9[a]**	**111.1**	**This work**
PPy@MOF-545-Co	0.5M $KHCO_3$	-1.0	13	1
C60@MOF-545-Co	0.5M $KHCO_3$	-1.1	12.7	2
PCN-601	0.5M $KHCO_3$	-1.1	16.4	3
Zr/Ti-NB-Co	0.1M $KHCO_3$	-1.1	14.6	4
CoPc/GDY/G	0.1M $KHCO_3$	-0.85	10	5
TAPP(Co)-$B_{18}C_6$-COF	0.5M $KHCO_3$	-1.0	9.45	6
NiPc	0.5M $KHCO_3$	-1.0	16.5	7
HS-NiPc	0.5M $KHCO_3$	-1.0	20.2	7
Ni_5-PTF-1000	0.5M $KHCO_3$	-0.9	18.4	8
PCN-222(Fe)	0.5M $KHCO_3$	-0.8	1.06	9
F_6-PCN-222(Fe)	0.5M $KHCO_3$	-0.8	3.36	9
3D-Por(Co)-COF	0.5M $KHCO_3$	-1.1	15.5	10
NiPc-$Ni(NH)_4$	0.5M $KHCO_3$	-1.1	24.8	11

TT-Por(Co)-COF	0.5M $KHCO_3$	-0.7	7.28	12.
TTF-Por(Co)-COF	0.5M $KHCO_3$	-0.9	6.88	13

[a] at the full-cell valtage of 2.9V.

Table S5. REDOX potential of Vg in four proportional MOF at 0.2 M Na_2SO_4.

Sample	E_1(vs.RHE)/V	E_2(vs.RHE)/V
Vg-Por(Co)-MOF(1:1)	0.285	-0.132
Vg-Por(Co)-MOF(2:1)	0.214	-0.169
Vg-Por(Co)-MOF(5:1)	0.144	-0.171
Vg-Por(Co)-MOF(9:1)	0.109	-0.177

Table S6. Comparison of the turnover frequencies (TOFs) of various catalysts electroreduction.

Catalyst	Electrolyte	Product	Applied Potential (V vs.RHE)	Highest TOF (h^{-1})	Reference
Vg-Por(Co)-MOF(9:1)	0.5M $KHCO_3$	CO	-1.0	999	This work

Vg-Por(Co)-MOF(9:1)	**1M KOH**	**CO**	**2.9[a]**	**4576**	**This work**
NiPc-NiO_4	0.5M $KHCO_3$	CO	-1.2	2603	14
$CoCp_2$@MOF-545-Co	0.5M $KHCO_3$	CO	-0.9	777	15
Co-PMOF	0.5M $KHCO_3$	CO	-0.8	1656	16
PcCu-O_8-Zn	0.1M $KHCO_3$	CO	-0.7	1404	17
MOF-1992/CB	0.1M $NaHCO_3$	CO	-0.63	720	18
$Al_2(OH)_2$TCPP-Co	0.5M $KHCO_3$	CO	-0.7	200	19
TTF-Por(Co)-COF	0.5M $KHCO_3$	CO	-0.9	676	13
TT-Por(Co)-COF	0.5M $KHCO_3$	CO	-0.7	481	12

[a] at the full-cell valtage of 2.9V.

References

1. Z. Xin, J. Liu, X. Wang, K. Shen, Z. Yuan, Y. Chen and Y. Q. Lan, *ACS Appl. Mater. Interfaces*, 2021, **13**, 54959-54966.

2. X. Dong, Z. Xin, D. He, J. L. Zhang, Y. Q. Lan, Q. F. Zhang and Y. Chen, *Chinese Chemical Letters*, 2022, DOI: 10.1016/j.cclet.2022.04.057.

3. S. N. Sun, L. Z. Dong, J. R. Li, J. W. Shi, J. Liu, Y. R. Wang, Q. Huang and Y. Q. Lan, *Angew. Chem., Int. Ed.*, 2022, **61**, e202207282.

4. Y. Zhou, L. Zheng, D. Yang, H. Yang and X. Wang, *Adv Mater*, 2021, **33**, e2101886.

5. H. Gu, L. Zhong, G. Shi, J. Li, K. Yu, J. Li, S. Zhang, C. Zhu, S. Chen, C. Yang, Y.

Kong, C. Chen, S. Li, J. Zhang and L. Zhang, *J. Am. Chem. Soc.*, 2021, **143**, 8679-8688.

6. S. An, C. Lu, Q. Xu, C. Lian, C. Peng, J. Hu, X. Zhuang and H. Liu, *ACS Energy Lett*, 2021, **6**, 3496-3502.

7. X. Wang, Y. Fu, D. Tranca, K. Jiang, J. Zhu, J. Zhang, S. Han, C. Ke, C. Lu and X. Zhuang, *ACS Appl. Energy Mater.*, 2021, **4**, 2891-2898.

8. Q. Wu, J. Liang, Z. L. Xie, Y.-B. Huang and R. Cao, *ACS Mater. Lett.*, 2021, **3**, 454-461.

9. X. Yang, Q. X. Li, S. Y. Chi, H. F. Li, Y. B. Huang and R. Cao, *SmartMat*, 2022, **3**, 163-172.

10. S. Y. Chi, Q. Chen, S. S. Zhao, D.-H. Si, Q. J. Wu, Y. B. Huang and R. Cao, *J. Mater. Chem. A*, 2022, **10**, 4653-4659.

11. M. D. Zhang, D. H. Si, J. D. Yi, Q. Yin, Y.-B. Huang and R. Cao, *Sci. China Chem.*, 2021, **64**, 1332-1339.

12. Q. Wu, M. J. Mao, Q. J. Wu, J. Liang, Y. B. Huang and R. Cao, *Small*, 2021, **17**, e2004933.

13. Q. Wu, R. K. Xie, M. J. Mao, G. L. Chai, J.-D. Yi, S. S. Zhao, Y. B. Huang and R. Cao, *ACS Energy Lett.*, 2020, **5**, 1005-1012.

14. J. D. Yi, D. H. Si, R. Xie, Q. Yin, M. D. Zhang, Q. Wu, G. L. Chai, Y. B. Huang and R. Cao, *Angew. Chem., Int. Ed.*, 2021, **60**, 17108-17114.

15. Z. Xin, Y. R. Wang, Y. Chen, W. L. Li, L. Z. Dong and Y. Q. Lan, *Nano Energy*, 2020, **67**.

16. Y. R. Wang, Q. Huang, C. T. He, Y. Chen, J. Liu, F. C. Shen and Y. Q. Lan, *Nat. Commun.*, 2018, **9**, 4466.

17. H. Zhong, M. Ghorbani-Asl, K. H. Ly, J. Zhang, J. Ge, M. Wang, Z. Liao, D. Makarov, E. Zschech, E. Brunner, I. M. Weidinger, J. Zhang, A. V. Krasheninnikov, S.

Kaskel, R. Dong and X. Feng, *Nat. Commun.*, 2020, **11**, 1409.

18. R. Matheu, E. Gutierrez-Puebla, M. A. Monge, C. S. Diercks, J. Kang, M. S. Prevot, X. Pei, N. Hanikel, B. Zhang, P. Yang and O. M. Yaghi, *J. Am. Chem. Soc.*, 2019, **141**, 17081-17085.

19. N. Kornienko, Y. Zhao, C. S. Kley, C. Zhu, D. Kim, S. Lin, C. J. Chang, O. M. Yaghi and P. Yang, *J. Am. Chem. Soc.*, 2015, **137**, 14129-14135.